Research Paper

Corundum formation by metasomatic reactions in Archean metapelite, SW Greenland: Exploration vectors for ruby deposits within high-grade greenstone belts

CrossMark

Chris Yakymchuk [a], Kristoffer Szilas [b],*

[a] Earth and Environmental Sciences, University of Waterloo, 200 University Ave West, Waterloo, Ontario N2L 3G1, Canada
[b] Geological Survey of Denmark and Greenland (GEUS), Øster Voldgade 10, 1350 Copenhagen K, Denmark

ARTICLE INFO

ABSTRACT

Corundum (ruby-sapphire) is known to have formed *in situ* within Archean metamorphic rocks at several localities in the North Atlantic Craton of Greenland. Here we present two case studies for such occurrences: (1) Maniitsoq region (Kangerdluarssuk), where kyanite paragneiss hosts ruby corundum, and (2) Nuuk region (Storø), where sillimanite gneiss hosts ruby corundum. At both occurrences, ultramafic rocks (amphibole-peridotite) are in direct contact with the ruby-bearing zones, which have been transformed to mica schist by metasomatic reactions. The bulk-rock geochemistry of the ruby-bearing rocks is consistent with significant depletion of SiO_2 in combination with addition of Al_2O_3, MgO, K_2O, Th and Sr relative to an assumed aluminous precursor metapelite. Phase equilibria modelling supports ruby genesis from the breakdown of sillimanite and kyanite at elevated temperatures due to the removal of SiO_2. The juxtaposition of relatively silica- and aluminum-rich metasedimentary rocks with low silica ultramafic rocks established a chemical potential gradient that leached/mobilized SiO_2 allowing corundum to stabilize in the former rocks. Furthermore, addition of Al_2O_3 via a metasomatic reaction is required, because Al/Ti is fractionated between the aluminous precursor metapelites and the resulting corundum-bearing mica schist. We propose that Al was mobilized either by complexation with hydroxide at alkaline conditions, or that Al was transported as K-Al-Si-O polymers at deep crustal levels. The three main exploration vectors for corundum within Archean greenstone belts are: (1) amphibolite- to granulite-facies metamorphic conditions, (2) the juxtaposition of ultramafic rocks and aluminous metapelite, and (3) mica-rich reactions zones at their interface.

1. Introduction

Corundum (Al_2O_3) is a relatively rare metamorphic mineral that requires unusual geochemical conditions of low silica activity combined with high aluminum contents of the host rock. Corundum in its purest form is colorless, but when trace element impurities of Cr, Fe or V enter the structure, corundum can become the colored gem ruby (red) or sapphire (blue), although other colors are also possible (e.g., Simonet et al., 2008). High quality gem ruby can be as expensive as diamond (e.g., Shor and Weldon, 2009);

hence it is of economic interest for mineral exploration companies, as well as for small-scale miners.

A major concern for gemologists is to identify the origins of gem quality corundum in order to control the trade of ruby and sapphire to avoid illegal activities. In recent years, several analytical methods have been employed with the aim of fingerprinting the origins of cut gem stones, including oxygen isotope analysis, Raman spectroscopic analysis (for inclusions), and *in situ* trace element analysis (e.g., Porto and Krishnan, 1967; Giuliani et al., 2005, 2014; Pornwilard et al., 2011). It has been demonstrated that corundum from Greenland has a rather unique composition in a global context, including mantle-like O-isotope compositions and elevated Cr and Si, which allows for precise fingerprinting of cut gems originating from the North Atlantic Craton (Thirangoon, 2008; Keulen and Kalvig, 2013). This specific signature reflects

the unusual geologic conditions in which Greenlandic ruby has formed, as we will give examples of in this paper.

One of the fundamental issues relevant for corundum prospecting is to identify the combination of rock types and metamorphic environment that favors its formation. Many of the most economic ruby occurrences are placer deposits sourced from marbles hosting corundum or alkaline dykes containing corundum xenocrysts (e.g., Sutherland et al., 1998; Garnier et al., 2008; Groat et al., 2014). In metamorphic terranes, proposed mechanisms for corundum stabilization include hydrothermal alteration (e.g., Bottrill, 1998), metasomatic exchange of silica with the ultramafic rocks (e.g., Riesco et al., 2005), and anatexis of aluminous protoliths accompanied by melt loss (e.g. Cartwright and Barnicoat, 1986; Palke et al., 2017).

In the present study, we highlight a less common primary geological environment of corundum formation, namely high-grade Archean greenstone belts. We present two case studies from southern West Greenland, where ruby corundum is hosted by aluminous Archean metapelite. Thermodynamic modelling is used to show under which pressure, temperature and geochemical conditions such rocks can stabilize corundum, and we demonstrate the critical importance of associated ultramafic rocks, which act as chemical buffers to maintain a low silica activity in the system. We summarize our findings by proposing several exploration vectors for corundum deposits within Archean greenstone belts, which may have applications for similar geological environments globally.

2. Geologic setting

The main portion of the North Atlantic Craton occurs along the SW coast of Greenland (Fig. 1). It is dominated by high-grade grey orthogneiss of the tonalite-trondhjemite-granodiorite (TTG) suite, although greenstone belts and fragmented anorthosite complexes also comprise an important component (e.g., Windley and Garde,

2009). Given that the Archean greenstone belts in this region have all experienced amphibolite- to granulite-facies metamorphism (e.g., McGregor and Friend, 1992; Garde, 1997), the neutral term 'supracrustal belt' has traditionally been preferred for such rock associations, and we therefore use this 'local' nomenclature here.

The geodynamic environment of formation for Archean crust is debated and still controversial within the geologic community. Some researchers argue that uniformitarian principles can be applied back into the Eoarchean (e.g., Polat et al., 2002; Komiya et al., 2015) or even the Hadean (Harrison et al., 2005; Watson and Harrison, 2005; Hopkins et al., 2008), while others argue that modern-style plate tectonics did not operate until the Mesoarchean (Smithies et al., 2007; Dhuime et al., 2012) or perhaps even the Neoproterozoic (Brown, 2008; Stern, 2008; Hamilton, 2011). There are several Archean cratons which clearly did not form by uniformitarian processes, one such example being the East Pilbara Craton (Collins et al., 1998; Van Kranendonk et al., 2004). However, the North Atlantic Craton may represent the opposite case, in which even the oldest component potentially formed via geologic processes resembling those of modern-style subduction zone systems. The currently favored model for the formation of the Archean continental crust in Greenland is by subduction (e.g., Nutman et al., 1996, 2015; Garde, 1997), and it is also the preferred interpretation for the formation of supracrustal belts (e.g., Garde, 2007; Polat et al., 2008; Jenner et al., 2009; Szilas et al., 2012, 2013, 2017), as well as for the associated anorthosite complexes of the North Atlantic Craton (Polat et al., 2009, 2012; Hoffmann et al., 2012; Huang et al., 2014). Although the question of the overall geodynamic environment is not the main topic of the present contribution, it does have some implications for the interpretation of the metamorphic evolution of the rocks describe and investigated in the present study.

Corundum is a high-grade metamorphic mineral that has been reported from several localities within Archean rocks in southern West Greenland. The best-known example is the extensive ruby
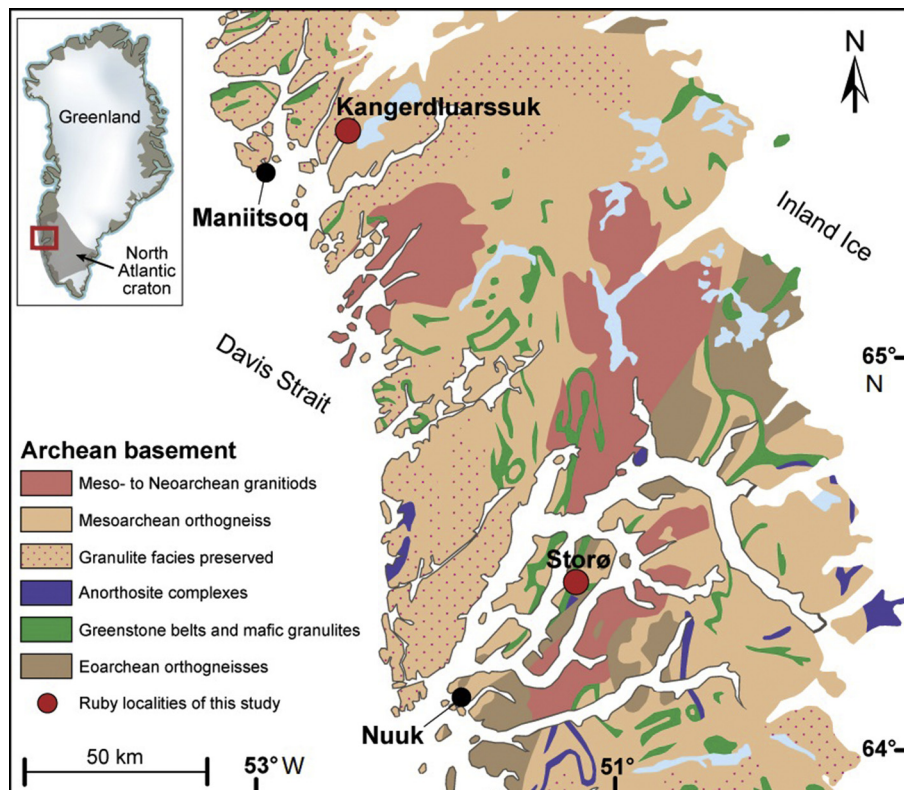

Figure 1. Geological map of the Maniitsoq and Nuuk regions of southern West Greenland. Based on mapping by the Geological Survey of Denmark and Greenland (GEUS).

deposits within the Fiskenæsset Anorthosite Complex (Myers, 1985; Polat et al., 2009), where corundum occurs along contacts between leucogabbro and ultramafic rocks and is interpreted to have formed during metasomatism at high-grade metamorphic conditions, although some occurrences also indicate the involvement of late tectonic granitic pegmatites (Keulen et al., 2014).

Minor corundum formation is also documented within the Eoarchean Itsaq Gneiss Complex (Appel et al., 2002; Lowry et al., 2003). In this case oxygen isotopes indicate an external fluid input to the system, where late metamorphic ruby corundum formed at the interface between amphibole-harzburgite and intrusive granitoid sheets.

Less well-known corundum occurrences are present on the island of Storø in the Nuuk region (Van Gool, 2006), where the mineral occurs within mica schist at the contact between metapelites and ultramafic rocks (Fig. 2). The Storø Supracrustal Belt (SSB) has received much attention due to the presence of gold mineralization hosted by sheeted quartz veins within amphibolites (see a summary in Scherstén et al., 2012). The maximum age of the SSB is constrained at ca. 2800 Ma by U-Pb dating of detrital zircon in quartzite (Scherstén et al., 2012; Szilas et al., 2014b). Re-Os isotope data on arsenopyrite demonstrates that the gold precipitated in quartz veins during regional metamorphism, and likely formed at two distinct events at ca. 2707 Ma and ca. 2640 Ma,

respectively (Scherstén et al., 2012). The aluminous garnet-sillimanite-biotite gneiss that appears to be the precursor for the corundum-bearing rocks on Storø (see Section 3) has been investigated intensely, because it was debated if this rock type represents a hydrothermal alteration product or simply a metapelite with a mafic source (e.g., Knudsen et al., 2007; Szilas and Garde, 2013; Szilas et al., 2016). Corundum formation in these rocks likely took place during peak metamorphic conditions at ca. 2635 Ma, given by U-Pb ages of zircon rims found consistently in all felsic rocks of the SSB (Hollis, 2005; Nutman et al., 2007; Van Gool et al., 2007). The Storø corundum occurrence is the first case study treated in the present work.

The second case study that we present in this contribution concerns a corundum occurrence in the Maniitsoq region (Garde and Marker, 1988), which is also hosted by metapelite juxtaposed with ultramafic rocks, which are high-grade amphibole-peridotites (Fig. 3). The Maniitsoq region was first studied extensively by Ramberg (1948), Sørensen (1954) and Berthelsen (1962), who documented several occurrences of ultramafic enclaves within orthogneiss as well as the presence of unusual metamorphic minerals such as corundum and sapphirine.

The tonalitic orthogneisses of the Maniitsoq and the Akia terrane have igneous ages of around 3 Ga (Garde et al., 2000; Windley and Garde, 2009). Dyck et al. (2015) presented a model
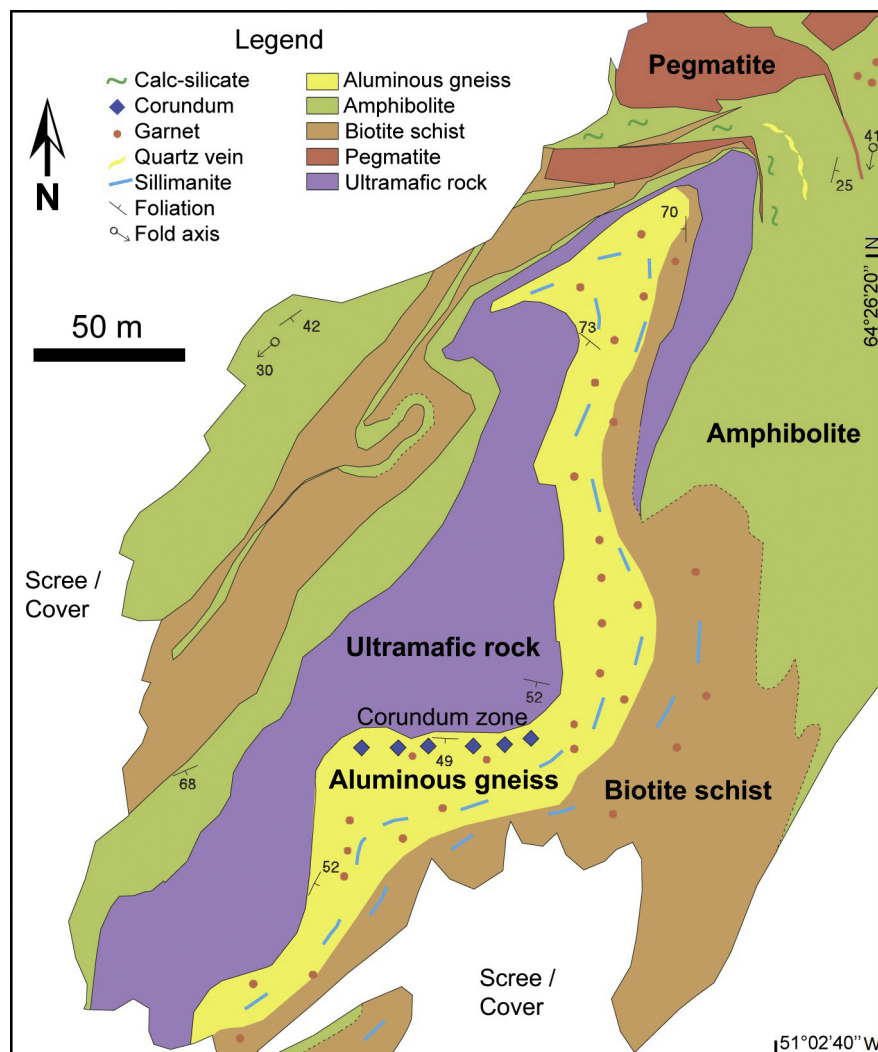

Figure 2. Detailed geological map of a part of the Storø Supracrustal Belt (SSB), Nuuk region, showing the corundum occurrence. Modified after Van Gool et al. (2007).
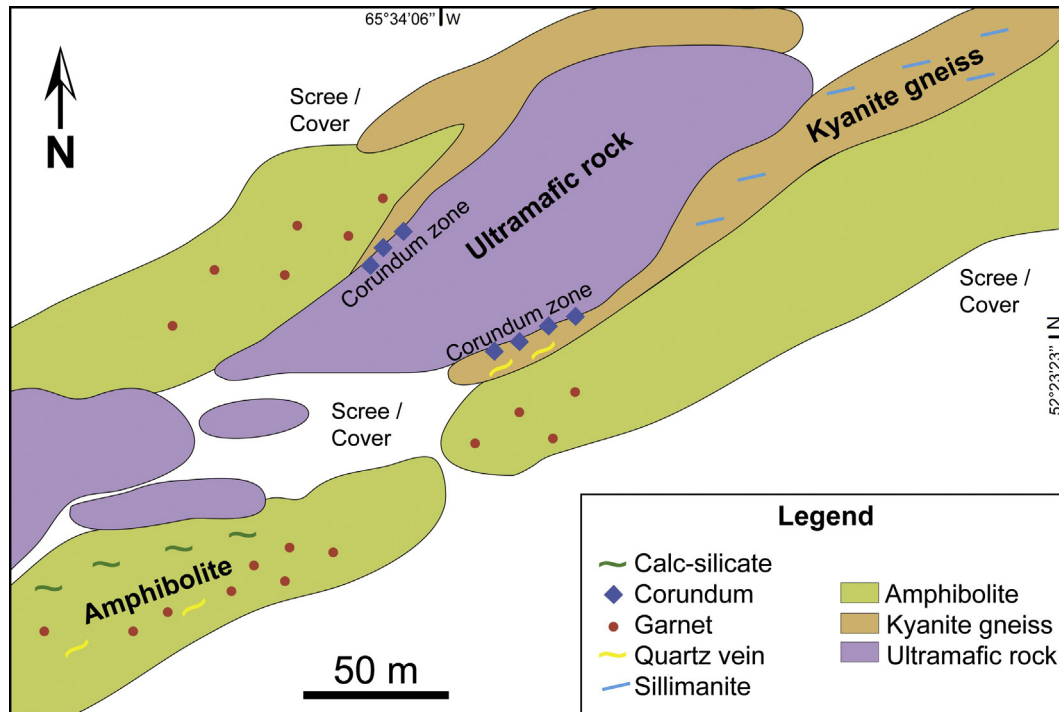
Figure 3. Detailed geological map of the corundum occurrence at Kangerdluarssuk, Maniitsoq region. Mapping based on our own field observations and satellite images.

for the Maniitsoq region where the area hosting corundum forms part of the so-called Majorqaq Belt, which was interpreted to represent lower crustal remnants of a Neoarchean orogen. Migmatitic metapelites from the Majorqaq Belt experienced a clockwise P-T evolution with peak metamorphic conditions of >810 °C at ∼9 kbar (Dyck et al., 2015). U-Pb ages of ∼2.56 Ga from anatectic zircon were interpreted by Dyck et al. (2015) to reflect the minimum age of the accretion of the Majorqaq Belt to the proto-North Atlantic Craton.

A controversial claim of a giant meteorite impact structure hosted by the Maniitsoq region has been proposed by Garde et al. (2014). However, several rebuttals to that claim have been put forth (e.g., Reimold et al., 2013, 2014), and given the small-scale focus of the present study, we will not discuss the meteorite impact model further in this work.

3. Field observations and petrography

3.1. Storø field observations

The island of Storø is located in the Nuuk region (Fig. 1) and it hosts the Storø Supracrustal Belt (SSB), which represents our first case study. Fig. 2 shows a detailed geologic map of the corundum occurrence within the SSB. The proximity of ultramafic rocks with aluminous rocks containing abundant garnet and sillimanite should be noted as a prospective setting for corundum formation.

A distinct type of schist is the host of the corundum and it occupies a less than 2-m-wide zone between the ultramafic rock and the aluminous gneiss. Fig. 4 shows examples of the three main lithological units in the SSB, namely amphibolite, biotite schist and aluminous gneiss as also seen on the detailed map in Fig. 2. Panels b, d and f in Fig. 4 shows the corundum-bearing mica schist found at the contact between the aluminous gneiss and the ultramafic rock of Fig. 2. The narrow mica schist that hosts corundum is generally less than 2 m wide and is thus not mappable even at this scale. Garnet is present within this rock on the side that is in contact

with the aluminous gneiss, whereas corundum is only present on the side of the mica schist that is in contact with the ultramafic rock. It should be noted that although the mica schist is present along the entire contact between the ultramafic rock and the aluminous gneiss, it is generally only a thin (<1 m) reaction zone with no corundum. Only where the mica schist forms a thicker unit of up to 3 m, does it contain corundum.

3.2. Maniitsoq field observations

The corundum-bearing Kangerdluarssuk locality in the Maniitsoq region (Fig. 1) has previously been described by Garde and Marker (1988) and Dyck et al. (2015). For simplicity, we refer to the Kangerdluarssuk locality, as the Maniitsoq ruby locality throughout this work to distinguish it from the Storø ruby locality. The detailed geologic map presented in Fig. 3 shows that corundum is only found along the contact between the ultramafic rocks and the kyanite-bearing metapelite. A few other occurrences are also reported by Garde and Marker (1988) at this locality, although they were not located during our own field work and thus not included in this map. Sapphirine has also been reported in the Maniitsoq region by Ramberg (1948) and Sørensen (1954). However, this mineral was not observed by us at any of the localities we visited during field work in the region.

At Maniitsoq we also sampled several amphibolites, for which we present geochemical data. These amphibolites are heavily modified containing calc-silicates and garnet-plagioclase veins and they are generally strongly sheared (Fig. 5e).

Fig. 5 shows examples of the three main lithological units at the Maniitsoq ruby locality (Kangerdluarssuk), namely amphibolite, kyanite gneiss and ultramafic rock as also seen on the detailed map in Fig. 3. Panels b, d and f in Fig. 5 shows the corundum-mica schist found at the contact between the aluminous gneiss and the ultramafic rock of Fig. 3. Fig. 5c shows a close-up of the ultramafic rocks adjacent to the corundum-bearing schist at the Maniitsoq locality. Note the brown unaltered peridotite patches between massive
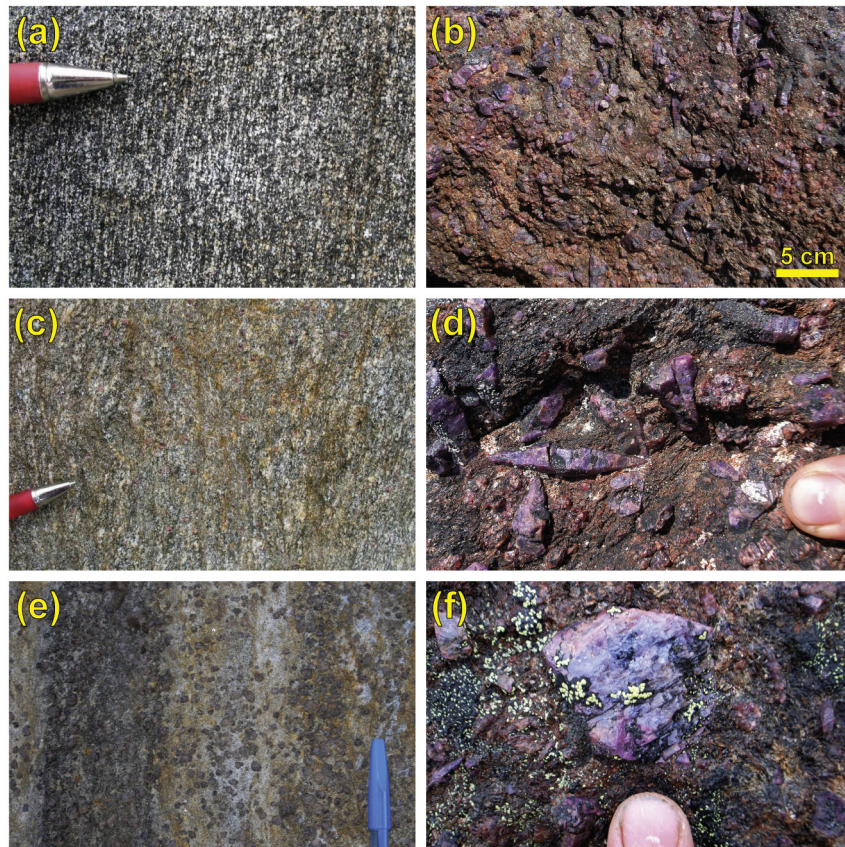
Figure 4. Field observations at the Storø corundum occurrence. (a) Amphibolite with foliation defined by elongate hornblende and plagioclase. (b) Ruby mica schist with up to 25% modal corundum. (c) Biotite schist with abundant sillimanite and garnet. (d) Close-up of an area shown in the upper right-hand corner of (b). Note the euhedral corundum crystals and the small rounded (corroded?) garnet porphyroblasts, which is present in the lower half of this photo. (e) Aluminous gneiss with distinct layers that are either biotite-rich (dark) or plagioclase- and sillimanite-rich (light). Garnet is dispersed throughout this rock. (f) Close-up on a cross-section of a large single corundum crystal that displays zoning with blue core (sapphire) and red-purple (ruby) rim.

tremolite veins, which are oriented orthogonally to the fracture orientations. In Table 1 we present geochemical data for both the unaltered (sample 455) and the amphibole-rich peridotites (samples 466 and 467).

3.3. Petrographic observations

The petrography of representative examples of the main lithological units relevant for the corundum formation at the Maniitsoq ruby locality are presented in Fig. 6. The peridotite consists mostly of olivine, spinel and orthopyroxene (Fig. 6a) with essentially no hydrous phases present, except for minor amphibole. This rock type is found at several localities in the Maniitsoq region, and detailed studies of similar rocks at Fiskefjord demonstrates these rocks to be represent cumulates related to dismembered layered intrusions (e.g., Szilas et al., 2015, 2018). The ultramafic rock or amphibole-rich peridotite *s.l.* is dominated by fine-grained tremolitic amphibole (Fig. 6b), and is found as an extensive network of fractures in proximity to the ruby mica schist.

Kyanite gneiss is comprised mainly of quartz, kyanite (Fig. 6c and d) and garnet with plagioclase, mica, amphibole and spinel as minor constituents. Centimeter-scale quartz-rich layers alternate with blueish fibrolitic kyanite-rich layers (Fig. 6c and d) and kyanite may comprise up ~40 vol.% of this rock type.

Ruby mica schist (Fig. 6e and f) consists mainly of biotite with corundum and plagioclase being the main other minerals in this rock type. Locally orthopyroxene, olivine and amphibole are also present. Corundum contains aligned inclusions of biotite,

indicating a relict foliation that is at a high angle to the main foliation. Mica also wraps around the corundum porphyroblasts, which suggests some deformation after corundum growth.

4. Methods

4.1. Bulk-rock geochemistry

Bulk-rock major and trace element data for the samples from the Maniitsoq region and the ruby mica schist from Storø were obtained from ALS Global laboratory in Ireland using their ME-MS61 procedure, which includes measurement by Inductively Coupled Plasma (ICP) methods. Below a brief summary of this method is given as it appears on ALS's website (www.alsglobal.com).

A prepared sample (0.25 g) is digested with perchloric, nitric, hydrofluoric and hydrochloric acids. The residue is topped up with dilute hydrochloric acid and analyzed by inductively coupled plasma-atomic emission spectrometry (ICP-AES). Following this analysis, the results are reviewed for high concentrations of bismuth, mercury, molybdenum, silver and tungsten and diluted accordingly. Samples meeting this criterion are then analyzed by ICP-MS, and results are corrected for spectral interelement interferences. Four acid digestions are able to dissolve most minerals; however, although the term "near-total" is used, depending on the sample matrix, not all elements are quantitatively extracted.

Bulk-rock geochemical data for the rocks from the SSB are from Szilas et al. (2016). One exception is sample 11801, which is the corundum-mica schist from this locality, which was also analyzed
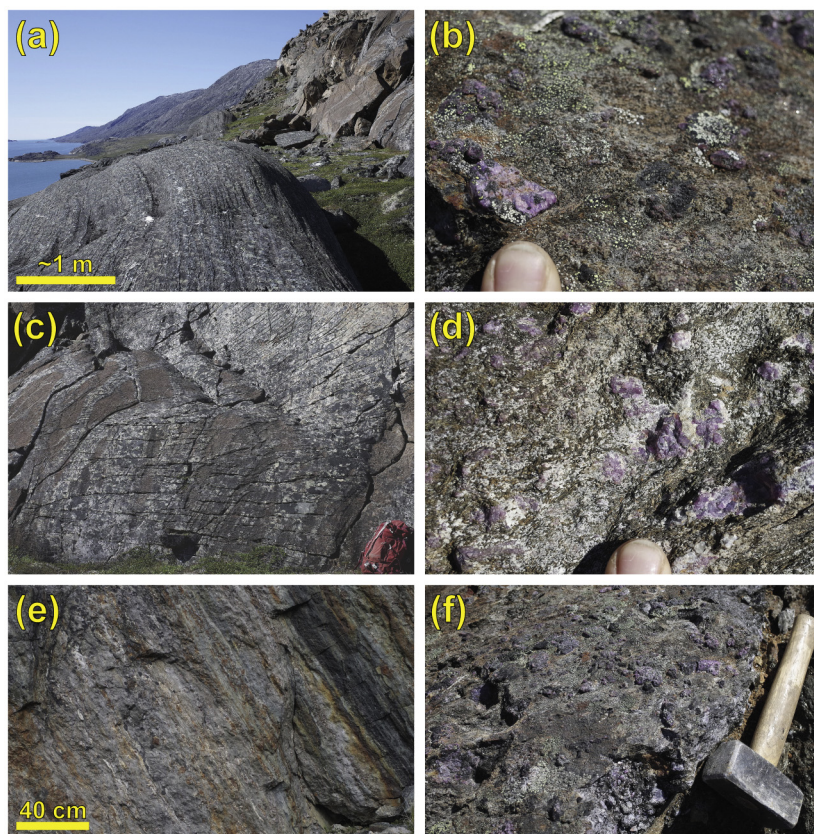
Figure 5. Field observations at the Maniitsoq corundum occurrence. (a) View of the kyanite gneiss with obvious layers defined by high modal contents of kyanite. The main ultramafic body is visible in the right-hand background. (b) Close-up of a corundum crystal in ruby mica schist. (c) Ultramafic rock showing white veins of amphibole, which increase in abundance towards the contact with the kyanite gneiss. Backpack for scale. (d) Ruby mica schist with obvious white patches of plagioclase, which commonly form around the corundum crystals and appears to be replacing them. (e) Banded diopside-rich leucocratic amphibolite with abundant plagioclase-garnet veins. (f) Ruby mica schist with about 15% modal corundum.

at ALS Global. All the new geochemical data are presented in Table 1 below and selected plots are shown in Figs. 7–9.

4.2. Computational methods

Phase equilibria modeling is used to (1) assess the pressure (P) and temperature (T) conditions of metamorphism, (2) explore the role of silica depletion on the mineral assemblage for the assumed precursors to the ruby-bearing rocks, (3) quantify the amount of silica depletion required to stabilize corundum, and (4) determine the amount and composition of melt expected at various P-T conditions and the composition of the residuum after melt loss. Calculations were conducted using THERMOCALC v.3.40 (Powell and Holland, 1988) using the internally consistent dataset (ds62) of Holland and Powell (2011). For the aluminous gneiss and biotite gneiss, modelling was undertaken in the MnO-Na$_2$O-CaO-K$_2$O-FeO-MgO-Al$_2$O$_3$-SiO$_2$-H$_2$O-TiO$_2$-Fe$_2$O$_3$ (MnNCKFMASHTO) chemical system using the activity-composition relations in White et al. (2014a,b). An amphibolite composition was investigated in the NCKFMASHTO chemical system using the activity-composition models from Green et al. (2016). Phases modelled as pure endmembers are quartz, rutile, titanite, aqueous fluid (H$_2$O), kyanite, sillimanite and corundum. In addition, one ultramafic composition was modelled in the NCFMASCrO chemical system using activity-composition models from Jennings and Holland (2015). The phases considered for the ultramafic composition include: liquid, plagioclase, clinopyroxene, olivine, spinel, chromite, garnet and orthopyroxene. Currently, models that include H$_2$O are not developed for ultramafic compositions. All mineral abbreviations are from Holland and Powell (2011) and are summarized in Table 2.

The phase equilibria modelling presented here considers both subsolidus and suprasolidus phase assemblages. For subsolidus assemblages, the system is assumed to be saturated in H$_2$O due to the prograde breakdown of hydrous minerals and the open-system behavior of H$_2$O with respect to subsolidus metamorphic systems (e.g., Guiraud et al., 2001; Webb et al., 2015). For suprasolidus phase assemblages, the system is not expected to be H$_2$O-saturated because any free H$_2$O is expected to partition into the melt phase (Huang and Wyllie, 1973; Thompson, 1982; Clemens and Vielzeuf, 1987; White and Powell, 2002; White et al., 2005). Therefore, for suprasolidus equilibria, the H$_2$O concentration of each composition was assigned so that the modelled bulk compositions have no free H$_2$O in the system (e.g., all H$_2$O in the composition is bound in the crystal structure of hydrous minerals) at the solidus at a specified pressure. For the samples from Storø, this pressure was set at 7 kbar, given the minimum estimate of Persson (2007) by garnet-biotite-plagioclase thermobarometry of rocks in the SSB recording temperatures of 521–624 °C and pressures of 4.5–6.1 kbar, which likely represent retrograde overprinting (minimum conditions). For the samples from Maniitsoq, the solidus was saturated with H$_2$O at 10 kbar, which is similar to the calculations by Dyck et al. (2015) for amphibole-kyanite-bearing metapelites at Maniitsoq. If the modelled heating path crossed the solidus at lower or higher pressures, the quantity of melt produced will be slightly overestimated and underestimated, respectively, and minor variation in the phase assemblages are expected.

Table 1

Bulk-rock geochemical data for the Maniitsoq rocks and one ultramafic ruby schist from Storø (sample 11801). Major elements are in wt.%, trace elements are in ppm. Blank values are below the limit of detection.

Sample#	454	455	456	457	458	459	460	461	462	463	464	465	466	467	11801
Rock type	Amphibolite	Peridotite	Ruby mica schist	Calc-silicate amphibolite	Leuco-amphibolite	Ultramafic rock	Leuco-amphibolite	Leuco-amphibolite	Kyanite gneiss	Ruby mica schist	Ruby mica schist	Ultramafic rock	Ultramafic rock	Ultramafic rock	Ruby mica schist
Latitude (°N)	65.56196	65.56846	65.56835	65.56738	65.56753	65.56763	65.56760	65.56726	65.56879	65.56815	65.56813	65.56821	65.56809	65.56831	64.43788
Longitude (°E)	−52.4008	−52.3906	−52.3909	−52.3927	−52.3925	−52.3921	−52.3917	−52.3936	−52.3876	−52.3900	−52.3900	−52.3906	−52.3902	−52.3909	−51.0459
SiO_2	53.1	40.7	34.4	48.4	56.1	52.7	62.6	57.5	67.0	25.9	37.7	39.9	54.8	46.8	28.04
Al_2O_3	19.10	2.42	33.2	15.00	15.55	4.05	15.95	18.20	19.05	44.4	24.2	2.02	2.10	18.70	42.49
Fe_2O_3	7.02	9.38	7.38	10.20	11.70	8.93	10.20	13.35	8.99	9.83	6.96	9.57	5.38	5.64	8.00
CaO	11.90	0.14	1.05	15.20	9.56	2.64	3.12	5.50	2.56	2.99	3.48	0.09	8.60	10.80	3.82
MgO	5.88	44.4	13.05	7.14	5.21	27.3	1.88	3.73	1.94	7.03	16.60	44.0	24.7	12.45	9.09
Na_2O	0.62	0.02	0.94	0.68	0.28	0.03	1.84	0.42	0.22	0.30	0.61	<0.01	0.06	0.45	0.55
K_2O	0.30	<0.01	3.69	0.24	0.04	<0.01	1.19	1.07	0.35	3.77	6.16	0.03	<0.01	2.28	4.20
Cr_2O_3	0.14	0.83	0.10	0.06	0.06	0.18	0.12	0.07	0.09	0.20	0.21	0.79	0.41	0.18	0.12
TiO_2	0.35	0.05	1.17	0.61	0.67	0.06	0.62	0.68	0.93	1.38	0.90	0.04	0.08	0.05	2.29
MnO	0.21	0.28	0.08	0.21	0.26	0.15	0.21	0.21	0.18	0.05	0.04	0.07	0.07	0.38	0.05
P_2O_5	0.01	0.01	0.01	0.03	0.05	0.01	0.11	0.05	0.19	<0.01	0.01	<0.01	0.04	<0.01	0.02
LOI	0.46	1.56	3.05	0.84	0.12	3.37	0.29	0.05	0.01	2.61	2.86	1.86	2.82	1.41	1.63
Total	98.25	99.79	98.16	98.61	99.60	99.42	98.16	100.76	101.50	98.59	99.84	98.37	99.06	99.24	100.3
Ag	0.08	0.03	0.17	0.05	0.2	0.1	0.25	0.05	0.08	0.61	0.09	0.04	0.22	0.1	
As	15.1	1240	3.8	5.9	18.5	9.8	11.7	26.8	17.1	3.6	0.4	1500	16.1	22.7	
Ba	311	2	280	39	15.9	3.7	261	275	126	1010	981	2.3	1.9	821	470
Be	2.11		0.26	0.49	0.48	0.13	0.62	0.2	0.53	0.47	0.73		0.06	0.6	
Bi	0.19	0.66	0.07	0.14	0.01	0.45	0.27	0.08	0.1	0.25	0.1	0.76	0.48	0.16	0.07
Cd	0.58	0.11	0.08	0.22	0.23	0.3	0.39	0.29	0.1	0.1	0.32	0.1	1.3	0.61	
Ce	29	0.31	12.2	4.41	4.73	1.07	30.5	4.48	44.4	53.4	105	0.45	4.6	0.67	87.1
Co	53.9	134	32.4	46.5	51.4	116	61.1	52.2	32.8	40.4	81.5	134	81.8	49.1	78.0
Cs	52.6	0.23	111	0.85	0.79	0.38	18.85	10.3	3.41	101	181.5	0.23	0.13	67.9	45.3
Cu	2.6	2.1	6.5	16.9	119.5	39.1	101	37.3	37.5	100.5	2.4	2.6	28.3	1	4.00
Dy	1.47		0.89	2.53	2.64	0.29	3.03	3.49	3.39	3.63	4.74	0.13	0.51	0.11	8.50
Er	0.69		0.69	1.47	1.69	0.22	1.84	2.26	1.89	2.24	2.76	0.06	0.47	0.1	5.19
Eu	0.71		0.8	0.55	0.62	0.04	0.91	0.64	0.91	1.04	1		0.36	0.23	1.16
Ga	14.8	3.2	28.1	15.4	17.7	3.8	17.3	17.1	23.8	44.5	23.3	2.6	2.8	8.5	41.3
Gd	1.99	0.05	0.9	2.3	2.24	0.15	2.74	2.91	3.9	4.28	5.03	0.13	0.51	0.13	8.51
Ge	0.13	0.39	0.13	0.27	0.22	0.2	0.12	0.17	0.15	0.17	0.24	0.59	0.07	0.36	
Hf	1.1		4.1	0.4	0.7		2.3	0.1	2.2	5.3	5.9		0.1	0.1	8.1
Ho	0.27	0.02	0.21	0.56	0.59	0.05	0.55	0.74	0.7	0.75	0.91	0.02	0.13	0.04	1.88
In	0.032	0.011	0.03	0.055	0.058	0.013	0.029	0.05	0.046	0.024	0.051	0.014	0.022	0.015	0.025
La	17.6		7.6	1.2	1.4	0.6	17.7	2.5	22.6	30.6	58.8		1.9	0.6	46.8
Li	16.8	7.5	119.5	21.7	29.4	3.4	61.9	48.1	18.7	91.4	147.5	95.5	3.7	64	60.0
Lu	0.11		0.16	0.24	0.28	0.03	0.22	0.32	0.38	0.33	0.41		0.07		0.84
Mo	0.72	0.12	0.22	0.09	0.18	0.15	0.98	0.13	0.3	1.29	0.08	0.1	0.14		
Nb	2.5	0.2	4.3	1.1	1.1	0.1	2.7	0.2	0.7	2.2	3.8	0.1	0.2	0.1	13.3
Nd	14.1	0.2	7	3.4	4.3	0.6	13.3	4.2	21.5	23.4	38.5	0.2	2.6	0.4	45.0
Ni	337	2640	272	141	141	1450	242	160.5	138	210	815	2570	1270	300	558
Pb	61.3	0.8	54.2	4.6	5.8	1.2	26.8	11.8	7	68.8	58.1	1	1.9	26.5	7.00
Pr	3.99	0.05	1.78	0.75	0.8	0.12	3.33	0.88	5.57	6.38	11.35	0.06	0.65	0.1	10.75
Rb	25.3	0.1	116	7	1.1	0.3	53.2	14	10.8	135.5	254	0.3	0.2	90.7	199
Sb	0.08	2.75	0.11	0.2	0.09	0.06	0.21		0.06	0.06	0.07	3.05	0.08	0.05	63.3
Sc	22.1	11.1	33	43.9	48.6	13.9	32.5	52.1	39.2	56.4	49.4	8.7	13.5	19.3	61.0
Sm	2.65	0.04	1.21	1.31	1.50	0.10	2.81	1.62	3.57	5.3	6.32	0.04	0.54	0.08	8.91
Sn	1.8	0.7	1.1	0.9	0.4	0.4	0.6	0.2	0.2	1.2	2.2		0.5	0.5	1.0
Sr	525	2.7	124.5	82.5	38.6	8	133.5	82.7	60.9	201	114.5	1.2	7.1	94.2	247
Ta	0.2		0.35	0.09	0.1		0.2		0.06	0.24	0.36				0.80
Tb	0.25		0.12	0.41	0.38	0.05	0.44	0.46	0.57	0.61	0.76	0.01	0.08	0.02	1.32
Te		0.23				0.14	0.09	0.05		0.06		0.43	0.08	0.05	

(continued on next page)

Table 1 (continued)

Sample#	454	455	456	457	458	459	460	461	462	463	464	465	466	467	11801
Rock type	Amphibolite	Peridotite	Ruby mica schist	Calc-silicate amphibolite	Leuco-amphibolite	Ultramafic rock	Leuco-amphibolite	Leuco-amphibolite	Kyanite gneiss	Ruby mica schist	Ruby mica schist	Ultramafic rock	Ultramafic rock	Ultramafic rock	Ruby mica schist
Th	4.18	0.1	5.11	0.16	0.19	0.07	4.26	0.17	3.78	12.1	13.45	0.1	0.14	0.04	8.08
Tl	0.57		1.3	0.09	0.02	0.03	0.58	0.25	0.09	1.62	2.63			1.86	2.55
Tm	0.13			0.28	0.25		0.26	0.3	0.36	0.31	0.4		0.05		0.80
U	0.93		1.22		0.19	0.07	1.28	0.13	0.83	3.1	2.83		0.09		1.78
V	113	54	208	220	240	51	167	260	122	262	210	44	59	82	440
W	2.8	0.9	5.5	0.9	1.3	0.9	10.4	1.1	0.8	26.9	2.4	0.6	0.3	0.5	56.0
Y	6.2	0.6	4.4	13.9	15.1	1.6	15.6	16.7	18.4	8.8	16.5	0.7	3.7	0.9	51.3
Yb	0.85	0.16	0.72	1.64	1.83	0.23	1.72	2.32	2.42	2.10	2.66	0.11	0.45	0.13	5.31
Zn	125	139	159	108	83	61	55	71	38	165	124	111	41	182	309
Zr	45.2		152	6.4	19.2	1.0	89.2	3.5	86.3	203	220	0.7	3.8	1.5	284

The modelled compositions of the aluminous gneiss, biotite gneiss and amphibolite are median values of the range of bulk-rock compositions reported in Szilas et al. (2016) with obvious outliers removed. The compositions used in the modelling are summarized in Table 3.

The stability of oxide and silicate minerals in high-temperature metamorphic rocks is sensitive to the amount of ferrous and ferric iron in the bulk composition (e.g., Diener and Powell, 2010; Boger et al., 2012). For the samples from Storø, the biotite-schist was assumed to have 18% of iron as ferric, 15% of the iron was assumed to be ferric for the aluminous gneiss, and 14% of the iron was assumed to be ferric for the amphibolite based on titration data from Szilas et al. (2014b) for the same lithological units in the SSB. For the ruby mica schists from Storø and Maniitsoq, various proportions of ferric to ferrous iron are examined. For the kyanite gneiss from Maniitsoq, 15% of the iron was assumed to be ferric, similar to the value used for the Storø aluminous gneiss. For the peridotite composition from Maniitsoq, 5% of the iron was assumed to be ferric, given that olivine dominated the rock and only accommodates divalent iron.

The role of silica depletion on the stability of corundum for three samples from Storø (aluminous gneiss, biotite schist and amphibolite) and one sample from Maniitsoq (kyanite gneiss) was evaluated by starting with a relatively silica-rich composition ranging to a silica-depleted composition. Two sets of diagrams were calculated to evaluate the temperature and pressure sensitivity of corundum-bearing assemblages to silica content. The first set of diagrams was constructed at a fixed pressure of 7 kbar for samples from Storø (Figs. 10a, 11a and 12a) and 10 kbar for the sample from Maniitsoq (Fig. 14a), but for a range of temperatures and SiO_2 concentrations of the system. This is similar to the approach taken by Riesco et al. (2004) who evaluated silica-undersaturated rocks and corundum formation in the Susqueda Aureole in Spain. The second set of diagrams (Figs. 10b, 11b, 12b and 14b) was constructed at a fixed temperature of 800 °C at a range of pressure and SiO_2 concentrations of the system for samples from Storø and Maniitsoq.

The left side of each of the temperature–composition and pressure–composition phase diagrams in Figs. 10–12 and 14 represents the silica-rich bulk composition and the right side of each diagram is the silica-depleted composition. When corundum is predicted to be stable in the phase assemblage, the amount of corundum in oxide-molar proportions (approximately equivalent to volume proportion) is illustrated by dashed contours on the appropriate diagrams.

The changes in the proportions of the different phases for two different scenarios are illustrated using mode-temperature and mode-pressure diagrams in Figs. 10–12 for samples from Storø and in Fig. 14 for the kyanite gneiss from Maniitsoq. These diagrams represent two end-member scenarios. The first scenario assumes a constant pressure and composition, but temperature increases. This could represent the modification of the SiO_2 content of the rock during interaction with an adjacent ultramafic body followed by heating during metamorphism or a scenario whereby a silica-depleted protolith undergoes prograde metamorphism (e.g., Goliani, 1989). The second scenario assumes that the system was at a constant pressure and temperature and that SiO_2 was removed from the composition. This is a simplified model that could represent a rock adjacent to an ultramafic rock that has achieved thermal equilibrium but SiO_2 is diffusing into the neighboring ultramafic rock (e.g., Riesco et al., 2005).

The effect of the ratio of ferric to ferrous iron in the bulk composition for the ruby-bearing rocks from Storø and Maniitsoq are explored with temperature-composition phase diagrams in Figs. 13a and 16a. The left side of these diagrams reflects only ferrous iron and the right-hand side of these diagrams represents 50% ferric iron and 50% ferrous iron.
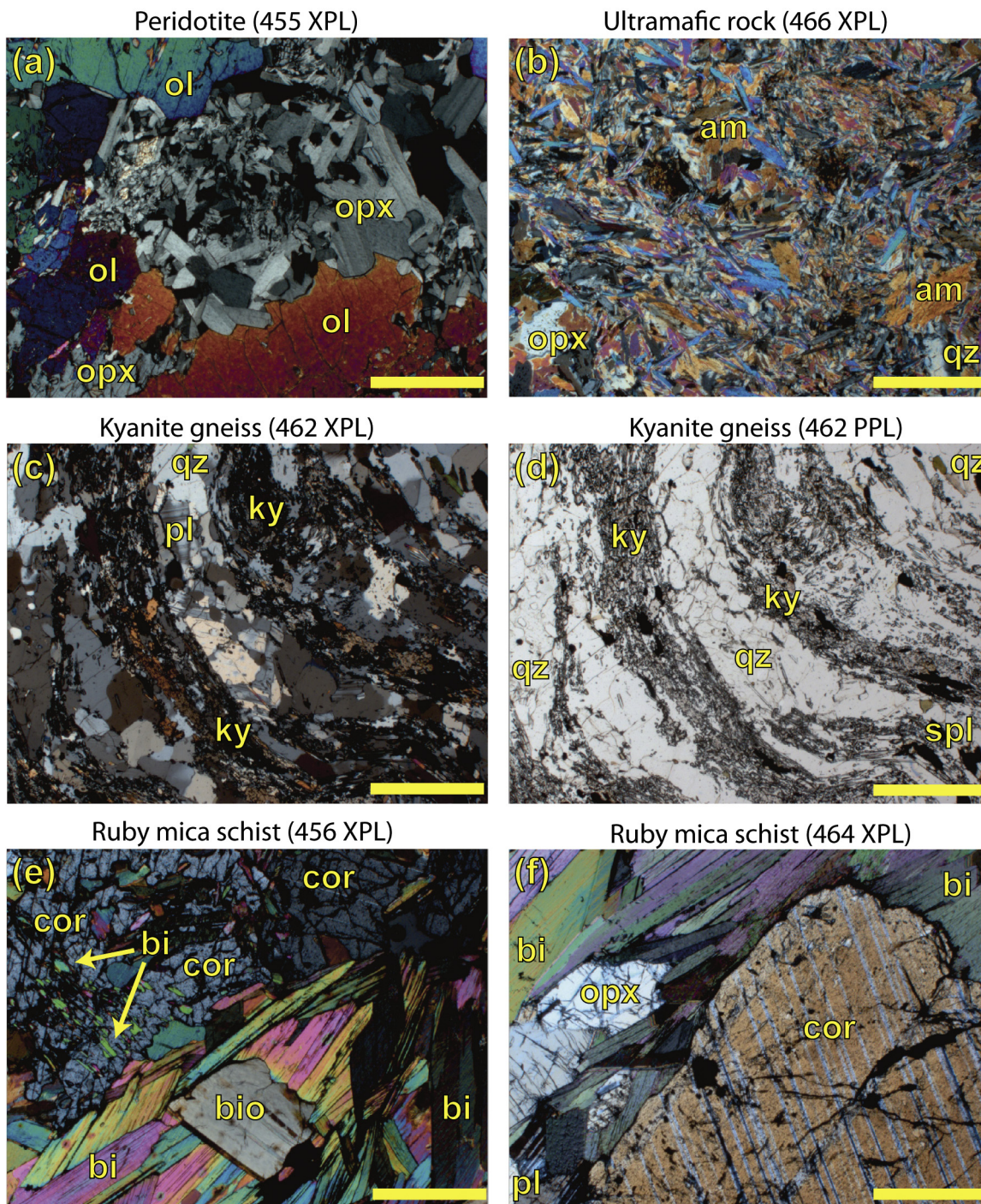
Figure 6. Petrographic microphotographs of the various rock types that are relevant for the corundum formation at the Maniitsoq ruby locality. (a) Unaltered peridotite showing olivine and orthopyroxene with essentially no hydrous phases present. (b) Hydrous ultramafic rock termed amphibole-rich peridotite in the field, although in detail it consists mostly of fine-grained amphibole. This rock represents the fracture network within the unaltered peridotite near the contact to the ruby mica schist. (c) Kyanite gneiss consisting of mostly quartz and kyanite. Locally garnet is also an important mineral and plagioclase, mica and spinel are only minor phases of this rock (d). Same image as in (c), but in plane polarized light. Fine-grained kyanite comprises up to 40 vol.% of this rock. (e) Example of ruby mica schist with aligned biotite inclusions in the corundum at a high angle to the main foliation. (f) Large corundum crystal showing characteristics lamellae. XPL: crossed polarized light. PPL: plane polarized light. Scale bars are 1 mm wide.

5. Results

5.1. Bulk-rock geochemical compositions

The new geochemical data for the Maniitsoq rocks are presented in Table 1 and Fig. 7 shows selected binary plots with trends towards the ruby-mica schists. The ultramafic rocks are generally Mg-rich and very depleted, although it should be noted that several samples, which are rich in amphibole (tremolite) also have distinctly elevated SiO_2 of up to 55 wt.%. The kyanite gneiss is rich in SiO_2 and Al_2O_3 with 67 wt.% and 19 wt.%, respectively. The ruby-mica schists are characterized by having unusually high Al_2O_3 of up to 44 wt.% in combination with very low SiO_2 of down to 26 wt.%. There is also strong enrichment in
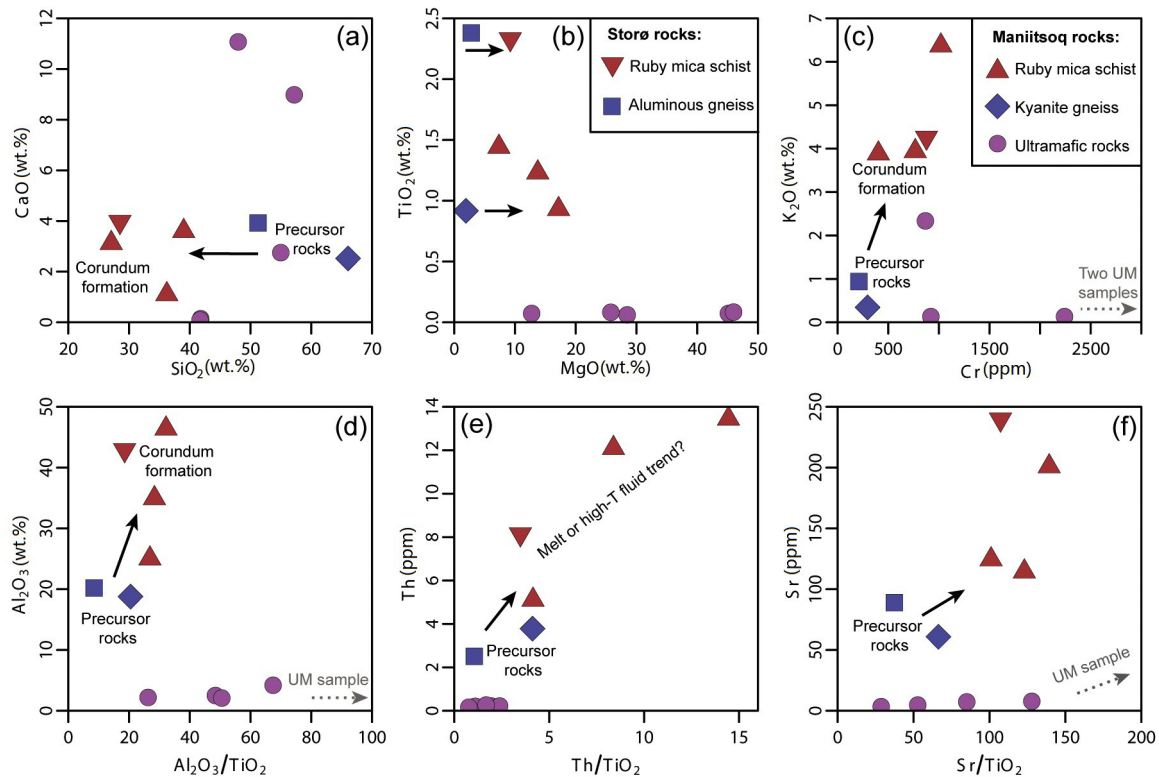
Figure 7. Bulk-rock geochemical diagrams. Oxides are in wt.% and trace elements are in ppm. (a) CaO vs. SiO$_2$ showing a significant drop in silica content from the precursor rocks to the corundum-bearing rocks. (b) TiO$_2$ vs. MgO showing a slight increase in MgO during the corundum formation. (c) K$_2$O vs. Cr showing a strong enrichment in potassium during the corundum formation, which is consistent with the abundant biotite in this rock. (d) Al$_2$O$_3$ vs. Al$_2$O$_3$/TiO$_2$ showing a strong enrichment in alumina for the corundum-bearing rocks. (e) Th vs. Th/TiO$_2$ showing a strong enrichment in Th for the ruby mica schists. (f) Sr vs. Sr/TiO$_2$ showing a strong enrichment in Sr for the ruby mica schist. The Storø aluminous gneiss is a median composition from Szilas et al. (2016) (see Table 3) and the rest of the data are from Table 1 of this study.

components such as Th, Sr and K$_2$O for the corundum-bearing rocks (Fig. 7).

Primitive mantle-normalized trace element patterns for the Maniitsoq rocks are shown in Fig. 8. It is seen that, although the abundances vary significantly, there are common features such as troughs for Ta-Nb-Ti, as well as both positive and negative anomalies for Sr and Eu.

The geochemistry of the Storø rocks have previously been described in detail by Szilas et al. (2014b, 2016) and will thus not be repeated here. However, the Storø rocks were interpreted to have formed in a geologic environment similar to a proximal arc-related basin, because the amphibolites consistently have negative Nb-Ta-Ti anomalies (also seen in Fig. 9), and metapelites generally have a strong mafic component suggesting immature sedimentary processing. However, mature quartzites (meta-sandstone) are also present, which indicates a proximal source with a provenance from continental crust. The geochemical difference between the biotite schist and the aluminous gneiss in the SSB were interpreted by Szilas et al. (2016) to mainly be controlled by the proportion of felsic versus mafic provenance, with the aluminous gneiss being derived almost entirely from a basaltic to ultramafic source.

The main geochemical features of the median aluminous gneiss and the ruby-mica schist at the Storø locality are shown in Fig. 7. The aluminous gneiss is characterized by having relatively high SiO$_2$ and Al$_2$O$_3$ of 51 wt.% and 20 wt.%, respectively, similar to the kyanite gneiss at the Maniitsoq locality. Both the Storø aluminous gneiss and the Storø ruby-mica schist have higher TiO$_2$ than any of the Maniitsoq rocks, which is consistent with overall higher abundances of incompatible trace elements as seen in Fig. 9.

5.2. Phase equilibria models for the Storø rocks

Phase equilibria modelling of the aluminous gneiss and biotite schist compositions from Storø indicate that quartz and corundum are not stable together at equilibrium. The depletion of silica is a requirement for corundum to stabilize in the equilibrium assemblage for both compositions. For example, at 7 kbar and 800 °C at suprasolidus conditions, the aluminous gneiss requires a decrease of ~6 wt.% SiO$_2$ to destabilize quartz and of ~7 wt.% SiO$_2$ to stabilize corundum (Fig. 12a and c). The biotite schist requires a more extreme reduction of SiO$_2$ in the bulk composition to destabilize quartz (~20 wt.% SiO$_2$) and stabilize corundum (~22 wt.% SiO$_2$) at the same temperature and pressure (Fig. 11a and d).

The quartz-out and corundum-in phase boundaries are not sensitive to pressure, except at $P < 7$ kbar in the stability field of cordierite for the biotite schist (Fig. 11b) and at $P < 6$ kbar in the stability field of cordierite or sapphirine for the aluminous gneiss (Fig. 12b). Corundum is not predicted to be stable at $P < 6$ kbar for the aluminous gneiss due to the breakdown of corundum to produce sapphirine. The quartz-out and corundum-in field boundaries are sensitive to temperature as indicated by the shift of both to lower SiO$_2$ values at higher temperatures (Figs. 11a and 12a). This indicates that less silica depletion is required to stabilize corundum at elevated temperatures for both the aluminous gneiss and the biotite schist.

With decreasing SiO$_2$ in both the aluminous gneiss and biotite schist, corundum modes increase relatively rapidly (e.g., closer spacing of contours in Figs. 11 and 12) during the concomitant breakdown of sillimanite (Figs. 11 and 12). Sapphirine is predicted to be stable at very low SiO$_2$ concentrations (Figs. 11 and 12) and
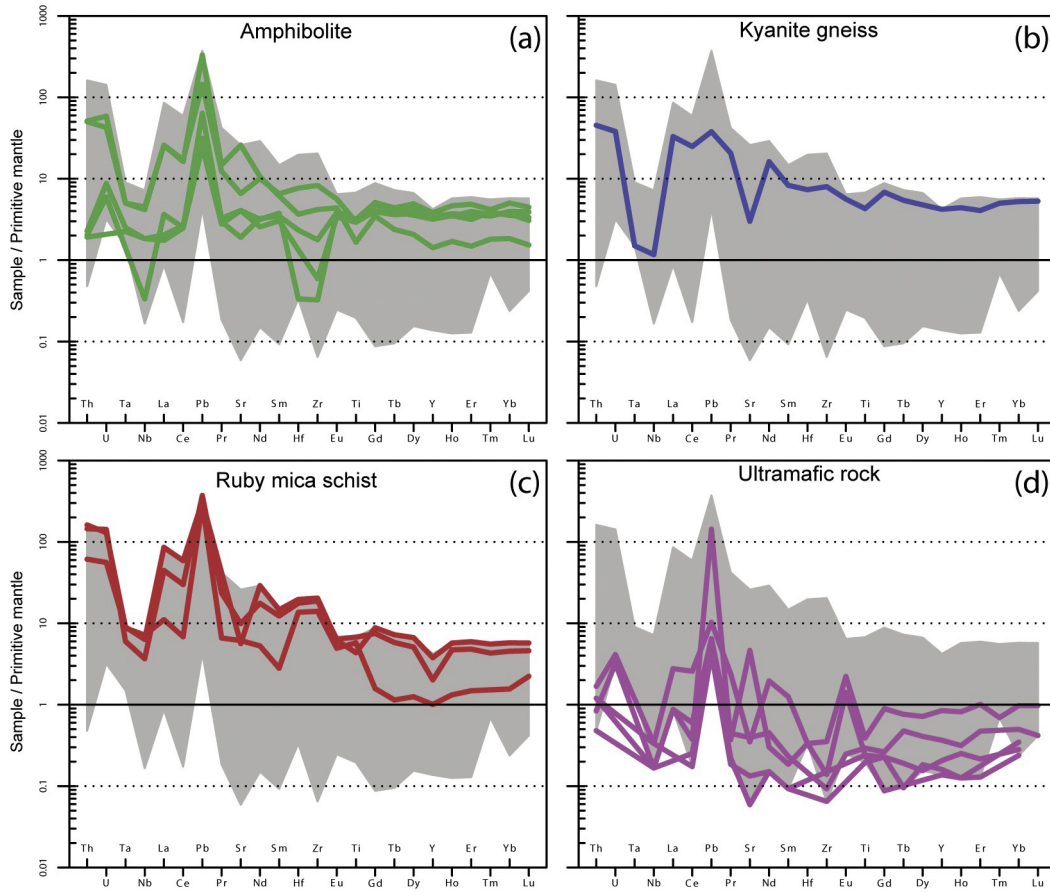
Figure 8. Maniitsoq rock types plotted on a primitive mantle-normalized (Palme and O'Neill, 2003) element diagram. (a) Amphibolites. (b) Kyanite gneiss. (c) Ruby mica schist. (d) Ultramafic rocks. The shaded area represents the total range of the Maniitsoq data (Table 1). Note the relative enrichment in Th-Zr-Hf-LREE from the kyanite gneiss to the ruby mica schists, which may suggest the involvement of melt transfer in the corundum-forming process.
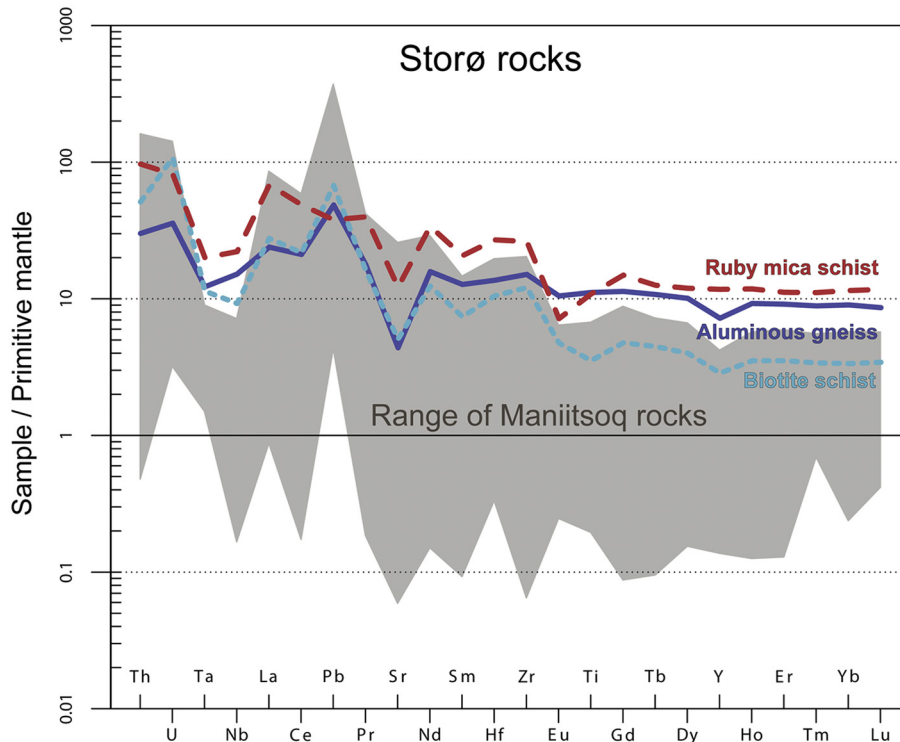

Figure 9. The Storø rocks plotted on a primitive mantle-normalized (Palme and O'Neill, 2003) element diagram. Median compositions of the biotite schist and the aluminous gneiss are based on data from Szilas et al. (2016) (see Table 3). The shaded area represents the total range of the Maniitsoq data for comparison (Table 1). Note that the Storø median amphibolite is not plotted, because it is not relevant for the corundum formation at this locality.

Table 2
Phase abbreviations used in the figures of the present study (from Holland and Powell, 2011).

aug	augite	liq	liquid
bi	biotite	ol	olivine
cd	cordierite	opx	orthopyroxene
cor	corundum	pl	plagioclase
g	garnet	q	quartz
H_2O	water	ru	rutile
hb	hornblende	sa	sapphirine
ilm	ilmenite	sill	sillimanite
ksp	K-feldspar	sp	spinel
ky	kyanite		

growth of sapphirine is modelled to occur at the expense of corundum (Figs. 11c, d and 12c, d). The maximum mode of corundum occurs at SiO_2 values just above those required for sapphirine stability.

The modelled amphibolite composition does not predict corundum formation even for extreme SiO_2 depletion (Fig. 10). For this composition, silica depletion results in the disappearance of quartz at 49–47 wt.% SiO_2 over the modelled range of pressure and temperature except at $T > 800$ °C and $P < 7$ kbar, where quartz is unstable even for the modelled median composition (Fig. 10a and b). Olivine is predicted to be stable at SiO_2 <42 wt.% for relatively low pressures at 800 °C (≤8 kbar; Fig. 10b). In general, the relatively low Al_2O_3 values of the amphibolite are expected to prohibit corundum formation due to SiO_2 depletion alone.

The predicted phase assemblage of the ruby mica schist is sensitive to the amount of ferric to ferrous iron in the bulk composition (Fig. 13a). For example, cordierite is expected to be stable in relatively oxidized rocks whereas spinel is stable in more reducing rocks (Fig. 13a). Corundum is stable over the modelled compositions but the amount of corundum is predicted to be

greatest at relatively oxidizing conditions at 800 °C (Fig. 13c). The observed mineral assemblage in the ruby mica schist from Storø includes garnet, biotite, ilmenite, plagioclase, corundum and spinel. Using the *P-T* phase diagram in Fig. 13b, this assemblage is restricted to $P > 5.5$–8 kbar with increasing temperature. This is broadly consistent with the previous estimates of the *P-T* conditions of metamorphism (Persson, 2007).

5.3. Phase equilibria models for the Maniitsoq rocks

Phase equilibria modelling of the kyanite gneiss from Maniitsoq also suggests that quartz and corundum are not stable together over the range of modelled *P-T* conditions, which is the same as the aluminous gneiss from Storø. At 800 °C, the first appearance of corundum is restricted to SiO_2 concentrations less than ∼40 wt.% over the range of modelled pressures. This requires the extraction of ∼15 wt.% SiO_2 from the starting kyanite gneiss (Fig. 14a). Note that the quartz-out and corundum-in field boundaries are not sensitive to temperature (Fig. 14a) or pressure, except at low pressures in the stability field of cordierite ($P < 6$ kbar; Fig. 14b). Corundum is expected to grow at the expense of kyanite or sillimanite (Fig. 14c and d).

When compared to the Storø composition, the kyanite gneiss from Maniitsoq requires more SiO_2 depletion to stabilize corundum, but it can potentially produce more. For example, the Maniitsoq composition is predicted to generate up to 30 mol.% corundum whereas the maximum amount of corundum in the Storø composition is ∼7 mol.% due to the growth of sapphirine at the expense of corundum at low SiO_2 contents (Fig. 12a and b). No sapphirine is predicted to be stable over the modelled conditions for the Maniitsoq kyanite gneiss (Fig. 14a and b).

The phase assemblage of the ruby mica schist from Maniitsoq is sensitive to the amount of ferric to ferrous iron in the bulk

Table 3
Compositions used in phase equilibria modelling including the new bulk-rock geochemical data for the Maniitsoq rocks, as well existing data for the Storø rocks from Szilas et al. (2016).

Median and measured compositions	wt.%										
	SiO_2	TiO_2	Al_2O_3	$Fe_2O_3^T$	MnO	MgO	CaO	Na_2O	K_2O	Cr_2O_3	%Fe^{3+}
Storø area											
Amphibolite	49.56	1.80	13.56	15.95	0.25	4.95	10.31	3.48	0.14	–	14
Aluminous gneiss	51.35	2.38	20.22	15.78	0.23	2.78	3.93	2.39	0.94	–	15
Biotite schist	68.72	0.75	14.52	6.79	0.06	2.91	1.60	2.08	2.56	–	18
Ruby mica schist	28.04	2.29	42.49	8.00	0.05	9.09	3.82	0.55	4.20	0.12	5
Maniitsoq area											
Kyanite gneiss	66.19	0.92	18.82	8.88	0.18	1.92	2.53	0.22	0.35	–	15
Ruby mica schist	39.01	0.93	25.04	7.20	0.04	17.18	3.60	0.63	6.37	–	15
Peridotite	41.76	0.05	2.48	9.62	0.29	45.55	0.14	0.02	0.01	0.07	5

| Modelled compositions		Figure	mol.%										
			H_2O	SiO_2	Al_2O_3	CaO	MgO	FeO^T	K_2O	Na_2O	TiO_2	MnO	O	Cr_2O_3
Storø area														
Amphibolite	x = 0	9	3.20	53.04	7.93	10.96	7.33	11.92	0.09	3.35	1.35	–	0.83	–
	x = 1	9	3.92	42.48	9.72	13.43	8.98	14.60	0.11	4.10	1.65	–	1.02	–
Aluminous gneiss	x = 0	11	1.01	60.78	12.00	4.24	4.18	11.95	0.61	2.33	1.81	0.19	0.90	–
	x = 1	11	1.41	45.52	16.67	5.89	5.81	16.60	0.84	3.24	2.51	0.26	1.25	–
Biotite schist	x = 0	10	2.86	72.65	8.57	1.72	4.34	5.12	1.64	2.02	0.57	0.05	0.46	–
	x = 1	10	5.43	48.12	16.27	3.26	8.24	9.71	3.10	3.83	1.08	0.10	0.87	–
Ruby mica schist	x = 0	12a	+	34.31	30.64	5.01	16.58	7.37	3.27	0.65	2.10	0.05	0.01	–
	x = 1	12a	+	33.10	29.56	4.83	15.99	7.11	3.16	0.63	2.03	0.05	3.55	–
	P–T	12b	+	34.25	30.59	5.00	16.55	7.35	3.27	0.65	2.10	0.05	0.19	–
Maniitsoq area														
Kyanite gneiss	x = 0	13	0.56	74.65	10.95	2.68	2.82	6.60	0.22	0.21	0.68	0.15	0.49	–
	x = 1	13	1.61	26.83	31.60	7.72	8.14	19.04	0.63	0.60	1.97	0.43	1.43	–
Ruby mica schist	x = 0	15a	+	41.47	15.68	4.10	27.22	5.76	4.32	0.65	0.75	0.04	0.01	–
	x = 1	15a	+	40.31	15.25	3.99	26.46	5.60	4.20	0.63	0.72	0.04	2.80	–
	P–T	15b	+	41.29	15.62	4.08	27.11	5.74	4.30	0.65	0.74	0.04	0.43	–
Peridotite	P–T	14	–	35.16	1.23	0.13	57.19	6.10	–	0.02	–	–	0.15	0.02

'+' in excess, '−' not considered.
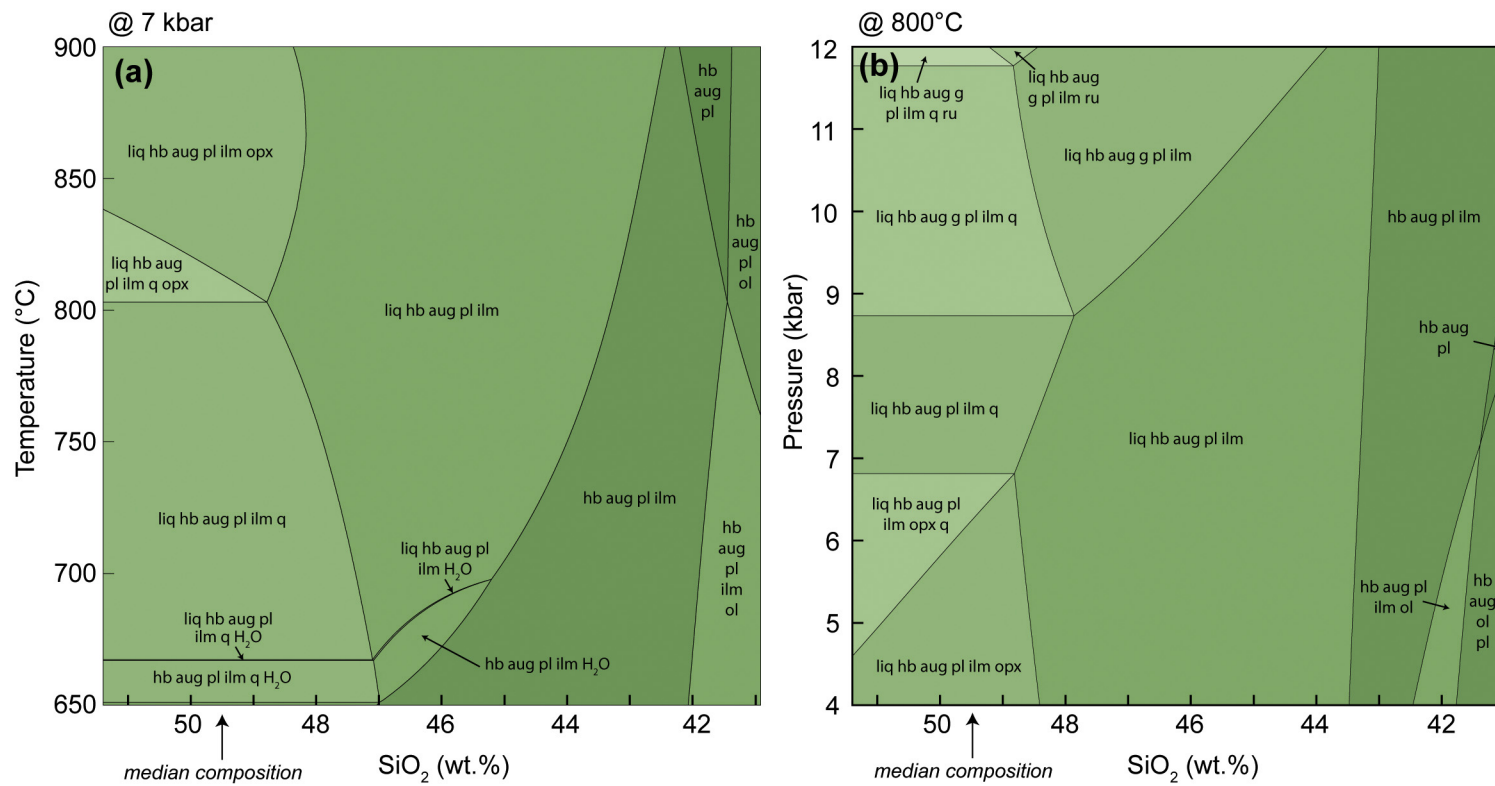
Figure 10. Storø amphibolite (for median composition see Table 3). (a) Temperature-SiO$_2$ diagram calculated for a fixed pressure of 7 kbar. (b) Pressure-SiO$_2$ diagram for the median amphibolite composition calculated for a fixed temperature of 800 °C. The median SiO$_2$ content is shown by the arrow on the horizontal axis. No corundum is expected to be stable in this composition across the modelled compositional range.
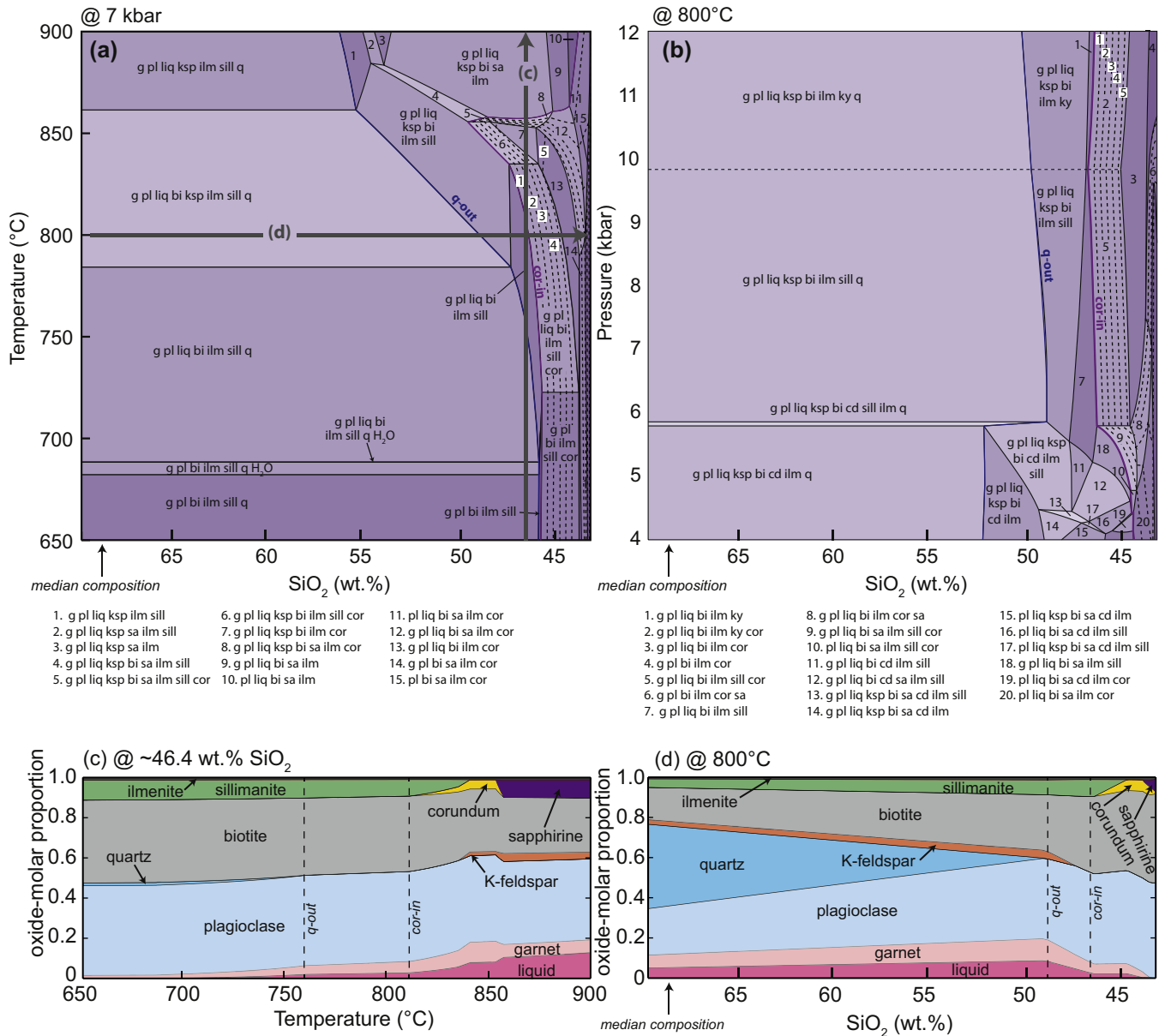
Figure 11. Storø biotite schist (for median composition see Table 3). (a) Temperature-SiO₂ diagram calculated for a fixed pressure of 7 kbar. (b) Pressure-SiO₂ diagram for the median biotite schist composition calculated for a fixed temperature of 800 °C. The median SiO₂ content is shown by the arrow on the horizontal axis. Contours represent the mode of corundum (∼vol.%). Quartz and corundum are never stable together. (c) Modebox diagram calculated at 46.4 wt.% SiO₂ for the Storø biotite schist composition over a range of temperatures. (d) Isothermal modebox diagram at 800 °C for various SiO₂ compositions of the biotite schist. The oxide-molar proportions are approximately equivalent to volumetric proportions (e.g., modes).

composition (Fig. 16a). Corundum is predicted to become unstable at temperatures just below the solidus for relatively reducing compositions but is stable at the solidus for more oxidizing composition. Similar to the composition from Storø, spinel growth at the expense of corundum occurs at relatively reducing conditions (Fig. 16c).

The observed mineral assemblage in the ruby mica schist from Maniitsoq includes garnet, biotite, plagioclase, corundum and spinel. Using the P-T phase diagram in Fig. 16b, this assemblage is restricted to P > 7.5–10 kbar with increasing temperature from 650 to 800 °C. Sapphirine is predicted to be stable at lower pressures, but this mineral was not observed in the Maniitsoq sample.

The peridotite from Maniitsoq is predicted to contain a stable assemblage of plagioclase, olivine, spinel and orthopyroxene (Fig. 15) over the range P-T conditions predicted for the ruby mica schist (Fig. 13). The absence of garnet from the peridotite restricts the

pressure to <14–15 kbar with increasing temperature from 700 to 900 °C, which is compatible with the P-T estimates of Dyck et al. (2015).

6. Discussion

6.1. Mechanism for corundum stabilization

Corundum-bearing rocks in metamorphic terranes can be produced by (1) hydrothermal alteration (e.g., Bottrill, 1998), (2) metasomatic exchange with the ultramafic rocks or rodingitization (e.g., Riesco et al., 2005) and (3) melt loss (e.g., Cartwright and Barnicoat, 1986). A corollary of these processes is that the chemistries of the nearby amphibolites at Maniitsoq are not appropriate for determining the geotectonic setting of formation. In the trace element diagram in Fig. 8a, some samples clearly have crustal
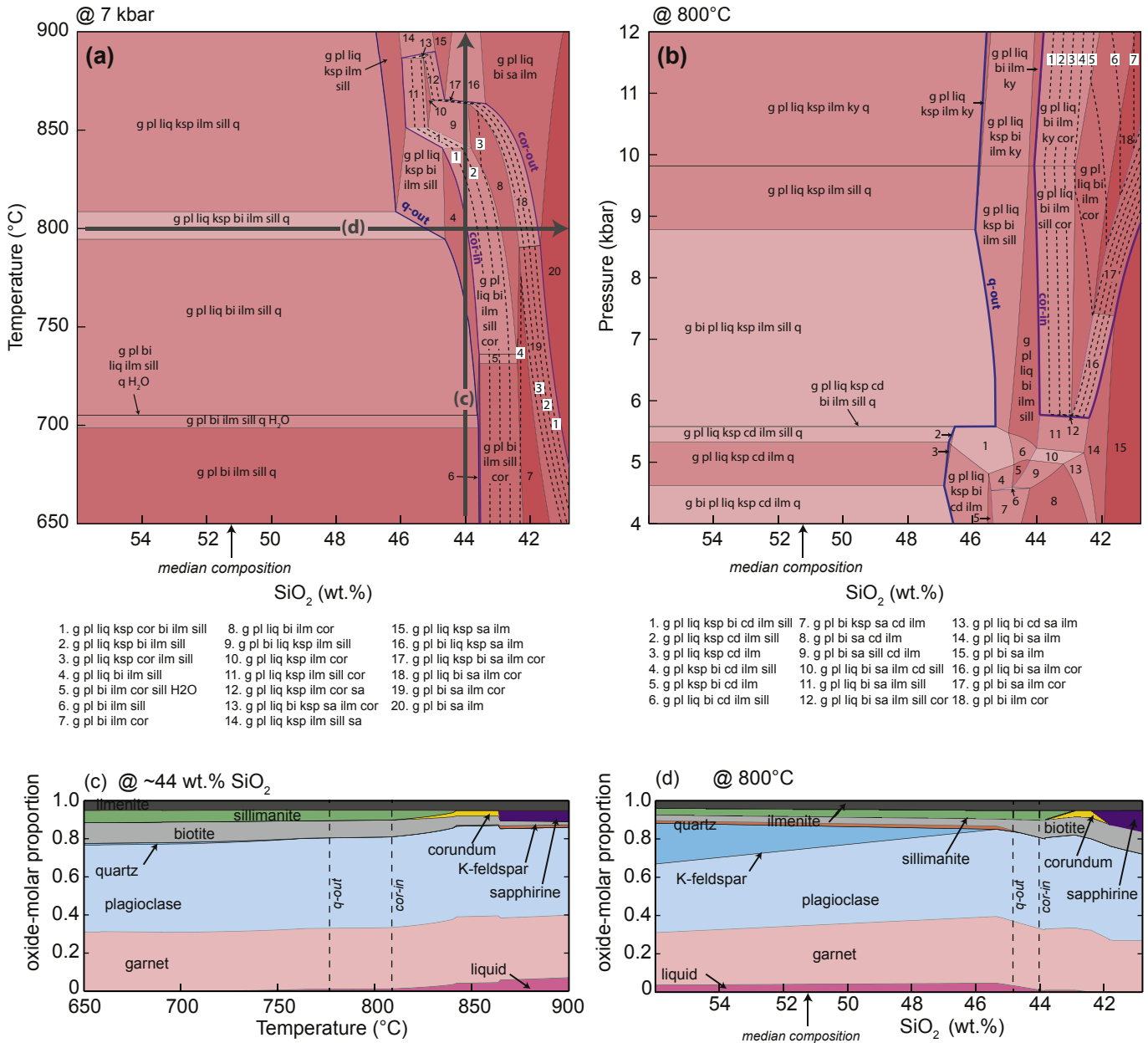
(a) @ 7 kbar

g pl liq ksp ilm sill
g pl liq ksp ilm sill q
g pl liq bi sa ilm
g pl liq ksp bi ilm sill
g pl liq bi ilm sill q
g pl bi liq ilm sill q H₂O
g pl bi ilm sill q H₂O
g pl bi ilm sill q
g pl liq ksp bi ilm sill q
cor-out
q-out
cor-in
median composition
SiO₂ (wt.%)

(b) @ 800°C

g pl liq ksp ilm ky q
g pl liq ksp ilm ky
g pl liq ksp ilm sill q
g bi pl liq ksp ilm sill q
g pl liq ksp cd bi ilm sill q
g pl liq ksp cd ilm sill q
g pl liq ksp cd ilm q
g bi pl liq ksp cd ilm q
g pl liq bi ilm ky
g pl liq ksp bi ilm ky
g pl liq ksp bi ilm sill
g pl liq ksp bi ilm sill cor
g pl liq bi ilm sill cor
g pl liq bi ilm sill
q-out
cor-in
median composition
SiO₂ (wt.%)

Legend (a):
1. g pl liq ksp cor bi ilm sill
2. g pl liq ksp bi ilm sill
3. g pl liq ksp cor ilm sill
4. g pl liq bi ilm sill
5. g pl bi ilm cor sill H2O
6. g pl bi ilm sill
7. g pl bi ilm cor
8. g pl liq bi ilm cor
9. g pl bi liq ksp ilm sill
10. g pl liq ksp ilm cor
11. g pl liq ksp ilm sill cor
12. g pl liq ksp ilm cor sa
13. g pl liq bi ksp sa ilm cor
14. g pl liq ksp ilm sill sa
15. g pl liq ksp sa ilm
16. g pl liq bi ksp sa ilm
17. g pl liq bi sa ilm cor
18. g pl liq bi sa ilm cor
19. g pl bi sa ilm cor
20. g pl bi sa ilm

Legend (b):
1. g pl liq ksp bi cd ilm sill
2. g pl liq ksp cd ilm sill
3. g pl liq ksp cd ilm
4. g pl ksp bi cd ilm sill
5. g pl ksp bi cd ilm
6. g pl liq bi cd ilm sill
7. g pl bi ksp sa cd ilm
8. g pl bi sa cd ilm
9. g pl bi sa sill cd ilm
10. g pl liq bi sa ilm cd sill
11. g pl liq bi sa ilm sill
12. g pl liq bi sa ilm sill cor
13. g pl liq bi cd sa ilm
14. g pl liq bi sa ilm
15. g pl bi sa ilm
16. g pl liq bi sa ilm cor
17. g pl bi sa ilm cor
18. g pl bi ilm cor

(c) @ ~44 wt.% SiO₂
ilmenite, sillimanite, biotite, quartz, plagioclase, garnet, corundum, K-feldspar, sapphirine, liquid; q-out; cor-in; Temperature (°C)

(d) @ 800°C
ilmenite, quartz, K-feldspar, sillimanite, plagioclase, garnet, liquid, biotite, corundum, sapphirine; q-out; cor-in; median composition; SiO₂ (wt.%)

Figure 12. Storø aluminous gneiss (for median composition see Table 3). (a) Temperature-SiO₂ diagram calculated for a fixed pressure of 7 kbar. (b) Pressure-SiO₂ diagram for the median aluminous gneiss composition calculated for a fixed temperature of 800 °C. The median SiO₂ content is shown by the arrow on the horizontal axis. Contours represent the mode of corundum (~vol.%). Quartz and corundum are never stable together. (c) Modebox diagram calculated at 44 wt.% SiO₂ for the Storø aluminous gneiss composition over a range of temperatures. (d) Isothermal modebox diagram at 800 °C for various SiO₂ compositions of the aluminous gneiss.

signatures with elevated La, Pb and Th relative to Nb and Ta, although two samples have flatter patterns. Thus, we will not make inferences about the geodynamic environment of formation based on these data, but will leave that discussion for a future study targeting Maniitsoq mafic rocks on a regional basis.

The role of hydrothermal alteration in the genesis of the corundum-bearing rocks can be assessed using the major and trace element chemistries. In Fig. 7 we show selected bulk-rock geochemical plot for the Storø and Maniitsoq rocks. Potassium and Sr are strongly enriched in the corundum-bearing rocks, which is hardly surprising due to their relatively volatile behavior during fluid-movement. It should be noted that TiO₂ is not generally much different between the metapelite precursor rocks and the corundum-bearing metasomatic products. Aluminum oxide versus TiO₂ is a ratio that is usually considered constant during hydrothermal alteration processes, because both elements have high field-strength (HFS) and are not easily mobilized. However, we observe that although TiO₂ is not significantly different for these rocks, they show a large difference in their Al₂O₃ contents and the corundum-bearing rocks even show a slight increase in this ratio despite TiO₂ actually being marginally higher in these. This suggests that Al₂O₃ was mobilized in these rocks, which either points to melt mobilization, alkaline hydroxide-complexation, or mobilization by alkali-bearing high-temperature fluids as Na-Al-Si-O polymers (e.g., Kerrick, 1988; Oelkers et al., 1994; Manning, 2006). Thorium is also a HFS element, which is not typically mobilized during hydrothermal processes. However, Kessel et al. (2005) demonstrated that Th can indeed become mobilized in high-temperature fluids or in a melt phase, as it is an incompatible
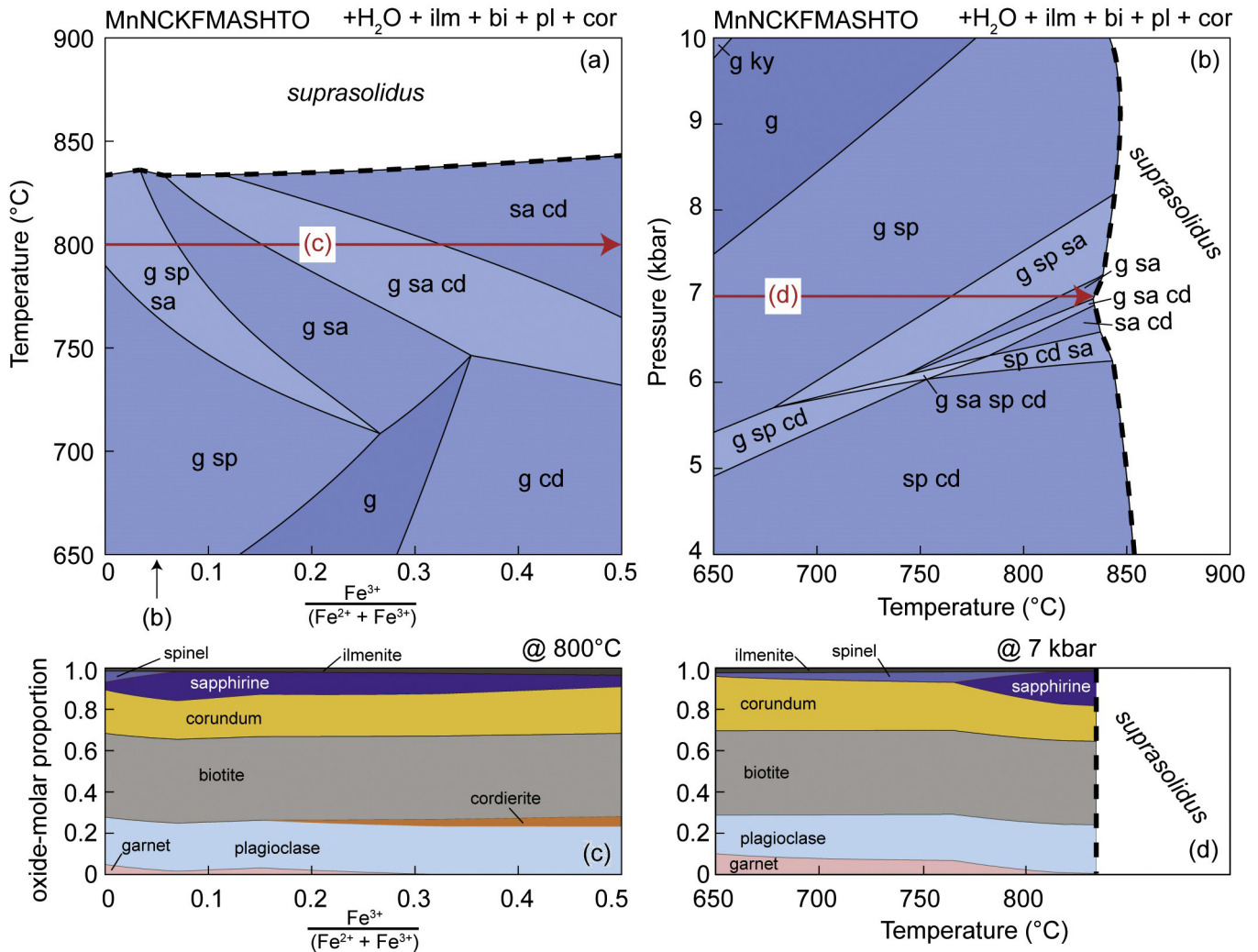
Figure 13. Storø corundum mica schist (sample 11801). (a) Temperature-composition diagram for various ratios of ferric to ferrous iron for the ruby mica schist from Storø calculated at a fixed pressure of 7 kbar. Corundum is stable across the entire diagram. (b) Pressure-temperature phase diagram for the ruby mica schist from Storø. (c) Composition-mode diagram illustrating the slight increase in the mode of corundum towards more oxidized compositions. (d) Temperature-mode diagram showing the decrease in the predicted mode of corundum towards higher temperatures.

trace element, which is also observed for mafic granulites in the Nuuk region (Szilas et al., 2014a).

An attempt was made to apply the isocon method of Grant (1986) to make mass-balance calculations for the metasomatic transformation from the metapelites at Storø and Maniitsoq to the protoliths of the corundum-bearing schists. However, this approach was not possible due to significant differences in the ratios of refractory elements between the metapelitic rocks and the resulting corundum schists. Thus, despite a close spatial proximity and a general similarity in trace element patterns between the sample pairs, the systematics of their high-field-strength elements, rule out simple hydrothermal alteration as a process to form a protolith suitable for corundum formation at higher metamorphic grade. This observation is compatible with three different explanations: either (1) partial melting was involved, which would fractionate fluid-immobile trace elements, and/or (2) mechanical mixing of pelite and ultramafic rocks during their juxtaposition resulted in erratic trace element ratios and differences to the actual protolith of the corundum-bearing schists making the isocon method inapplicable. (3) Alternatively, and perhaps the simplest explanation is that the metapelites were heterogeneous at a scale

that is smaller than the sampling and thus any primary mineralogical heterogeneity would also control the budget of immobile elements. Nonetheless, hydrothermal alteration is not the dominant process for generating corundum-bearing rocks at Storø and Maniitsoq.

Metasomatic exchange or diffusion of silica between silica-rich and silica poor rocks is a common origin for corundum-bearing rocks in high-grade gneiss terranes (e.g., Riesco et al., 2004, 2005). The driving force for diffusion in metamorphic and metasomatic systems is differences in chemical potential gradients of constituent components (e.g., White et al., 2008). For the ruby-bearing rocks, the difference in chemical potential of silica between the relatively silica-poor ultramafic rock and the adjacent silica-rich aluminous rocks is expected to be the principal factor. The juxtaposition of these rocks would result in a chemical potential gradient that could be equalized by the transfer of silica from the rock with the higher chemical potential (aluminous gneiss) to the rock with lower μ_{SiO_2} (ultramafic rock). Values of the chemical potential of SiO_2 for the different rock types were calculated with THERMOCALC. For Storø, the calculated chemical potential of SiO_2 (μ_{SiO_2}) at P–T conditions of 800 °C and 7 kbar of the ultramafic
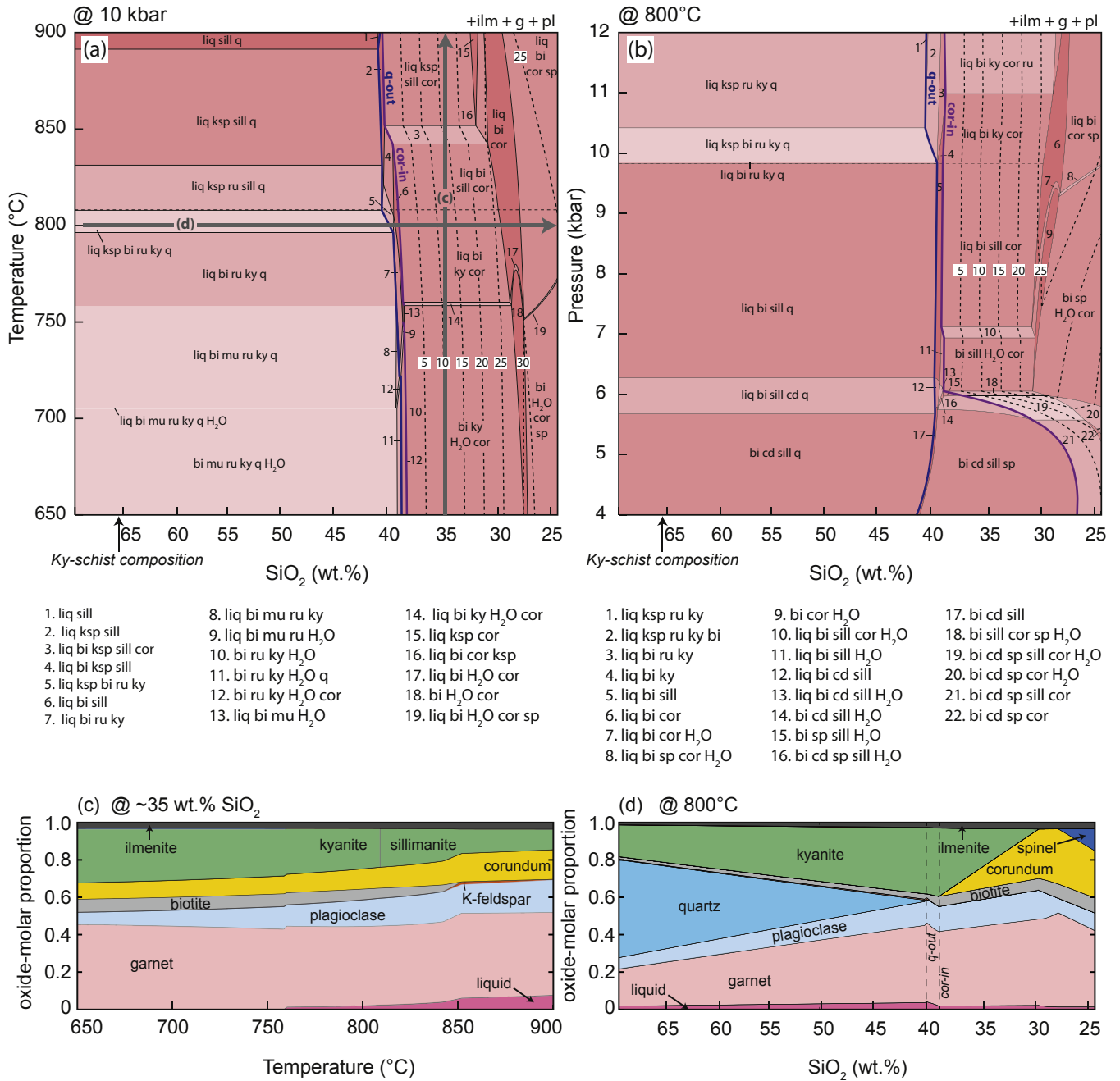
Figure 14. Maniitsoq kyanite gneiss (sample 462). (a) Temperature-SiO$_2$ diagram for the kyanite-schist composition from Maniitsoq calculated for a fixed pressure of 10 kbar. (b) Pressure-SiO$_2$ diagram for the kyanite-schist composition calculated for a fixed temperature of 800 °C. The median SiO$_2$ content is shown by the arrow on the horizontal axis. Contours represent the mode of corundum (~vol.%). Quartz and corundum are never stable together. (c) Modebox diagram calculated at 35 wt.% SiO$_2$ for the kyanite gneiss composition over a range of temperatures. (d) Isothermal modebox diagram at 800 °C for various SiO$_2$ compositions of the kyanite gneiss. The oxide-molar proportions are approximately equivalent to volumetric proportions (e.g., modes).

composition is −981.76 kJ/mol whereas it is a much higher value of −973.65 kJ/mol for the aluminous gneiss. The calculated value for the ruby-mica schist is −976.37 kJ/mol, which is in between the other two values. For Maniitsoq, the μ_{SiO_2} value at $P–T$ conditions of 800 °C and 10 kbar for the ultramafic composition is −975.95 kJ/mol. The kyanite-gneiss has a value of −966.64 kJ/mol and the ruby-bearing rock has an intermediate value of −972.57 kJ/mol. Both examples show that there is a strong gradient in chemical potential that develops at or near the peak of metamorphism between the ultramafic rock and the adjacent aluminous rocks. The ruby-bearing rocks are interpreted to represent a snapshot of the

system attempting to equilibrate this gradient by diffusion of silica from the relatively high − μ_{SiO_2} aluminous rocks towards the relatively low − μ_{SiO_2} ultramafic rocks. This is supported by the estimated intermediate μ_{SiO_2} values of the ruby-bearing rocks compared with the ultramafic rocks and aluminous gneisses.

Melt loss is an additional mechanism that may form corundum-bearing assemblages. The composition and proportion of melt for the Storø aluminous gneiss and Maniitsoq kyanite gneiss were modeled in THERMOCALC and the results are summarized in Fig. 17. The composition of the melt are those in equilibrium with both rock types at 700, 750, 800, 850 and 900 °C and the melt loss vectors
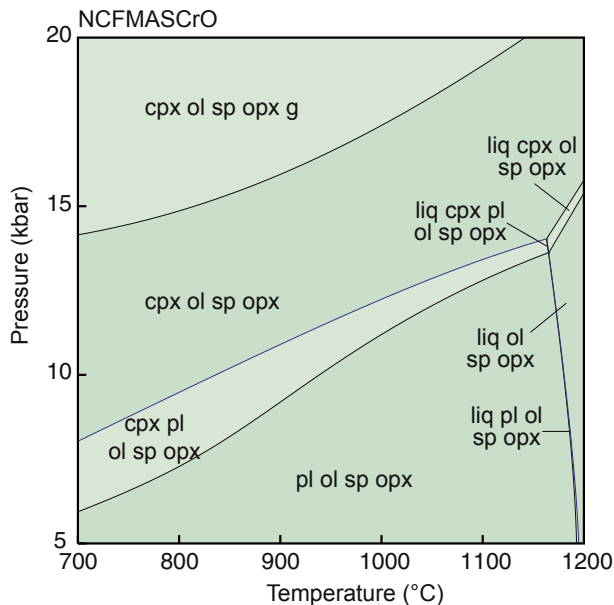
Figure 15. Maniitsoq peridotite (sample 455). Pressure-temperature phase diagram for a representative peridotite composition from Maniitsoq. Note that the mode is dominated by olivine followed by orthopyroxene (up to 17%), 1–3% spinel (containing ~1 mol.% Cr), and only minor plagioclase (<<1%).

represent the residuum composition after the extraction of 10 mol.% (roughly equivalent to 10 vol.%) melt from the system. This amount is considered a maximum because the calculated proportion of melt at the modeled $P–T$ conditions is generally <10 mol.% (Figs. 12c, d and 14c, d). Vectors representing the composition of the residue after melt loss plot towards the FeO + MgO apex and away from the SiO_2 apex in Fig. 17 resulting in slightly more residual compositions but not enough to account for the measured compositions of the corundum-bearing rocks. Nonetheless, melt loss may have made a minor contribution to reducing the silica content of the inferred protoliths.

The relative importance of melt loss and silica depletion during metasomatism and corundum formation is evaluated in Fig. 17. For the Maniitsoq sample, some combination of melt loss and silica depletion is plausible to explain the composition of the ruby-bearing rocks. The modelled compositions do not produce the measured compositions exactly, but it is the correct trajectory and within the range of the total variability of corundum-bearing mica schists at Maniitsoq. For the Storø aluminous gneiss, the melt loss vector is incompatible with the observed trends, and it should also be noted that the $P–T$ conditions for this sample do not support extensive partial melting. However, as seen in Fig. 9, the Storø ruby mica schist also appears to be enriched in Th-Zr-Hf-LREE relative to the aluminous gneiss precursor rock, which does indicate a role for melt transfer or alternatively a high-temperature supercritical fluid in which these elements behaved strongly incompatible. The ruby-mica schists may require prior Al_2O_3 enrichment (or FeO + MgO depletion) via hydrothermal leaching, however, the very large Al-enrichment observed in Fig. 7 requires significant mobilization either as Al-hydroxide complexes or as Na-Al-Si-O polymers (Oelkers et al., 1994; Manning, 2006).

It is important to note the large enrichment in silica in Fig. 17, from the most refractory peridotite (sample 455) to the most amphibole-rich peridotite (sample 466) at the Maniitsoq corundum locality. This clearly demonstrates that the buffering capacity of the ultramafic rocks with respect to silica is of great importance,

because it is of the same magnitude as would be required for the depletion of the aluminous precursor to the composition of the corundum mica schist protolith. We consider this observation to be strong evidence for the direct involvement of the ultramafic rocks in the metasomatic processes and the stabilization of corundum in metapelite. One way in which this transfer of silica into the ultramafic rocks could be envisaged to take place would be by fracture development during deformation associated with the transformation of serpentinite to peridotite. Alternatively, the silica transfer could have occurred during the formation of tremolite in the ultramafic rocks at higher temperature conditions. This would result in a significant volume decrease of the ultramafic rocks and fracturing of the surrounding metapelite to accommodate this volume change, which could induce fluid infiltration that would result in the mobility of primarily silica to form tremolite in the ultramafic rocks. Support for this model is seen by the extensive network of amphibole dominated fractures close to the contact between the ultramafic rocks and the kyanite gneiss (Fig. 5c).

Nevertheless, the loss of silica by itself cannot account for the strong enrichment in Al_2O_3 that is needed to stabilize corundum to the extent that is seen in the sample of the Storø ruby schist, where Al_2O_3 comprises up to 30 mol.% of the measured composition. Two ways of doing this are by either: (1) pre-metamorphic hydrothermal leaching of the aluminous gneiss, which would serve to cause residual enrichment in fluid-immobile components, or (2) by hydrothermal addition of Al-hydroxide complexes under highly alkaline conditions. The former is not supported because TiO_2, which would certainly have remained immobile, is generally within the same range between the metapelites and the corundum-bearing rocks at both Maniitsoq and Storø (see Fig. 7). The second option of introduction of Al-hydroxide complexes during hydrothermal alteration is rather speculative, but may be supported by the reducing and alkaline nature of serpentinization reactions (e.g., Frost, 1985; Klein et al., 2013). This is perhaps supported by the abundant calc-silicate minerals within the leucoamphibolites at Maniitsoq, such as epidote, diopside and garnet, which is typical of rodingitization, a process which requires abundant $Ca(OH)_2$ to be present in the fluids (Bach and Klein, 2009). Thus, it appears that there was a long and complex evolution of the fluids ranging from early seafloor hydration and formation of serpentine in the ultramafic rocks and later dehydration reactions with the formation of amphibole-peridotite (Fig. 6b), which was likely associated with the stabilization of corundum in the silica-depleted aluminous gneisses.

6.2. Limitations of modelling

The phase equilibria modelling presented here suggests that quartz and corundum do not form a stable assemblage together in relatively high-temperature metamorphic rocks. This contrasts with some reports of assemblages that include quartz + sillimanite + corundum (e.g., Guiraud et al., 1996; Shaw and Arima, 1998). Experimental work by Harlov et al. (2008) demonstrated that these assemblages are metastable, but may persist in metamorphic rocks due to sluggish kinetics. However, quartz in direct contact with corundum is relatively rare in natural samples and corundum + quartz assemblages are usually found in granulites with complex microstructures (e.g., White et al., 2008; Kelsey and Hand, 2015) that may not reflect hand-sample scale equilibrium, which is what we model here.

Phase equilibria modelling is a simplification of natural systems. Here, we investigate two occurrences of ruby from Storø
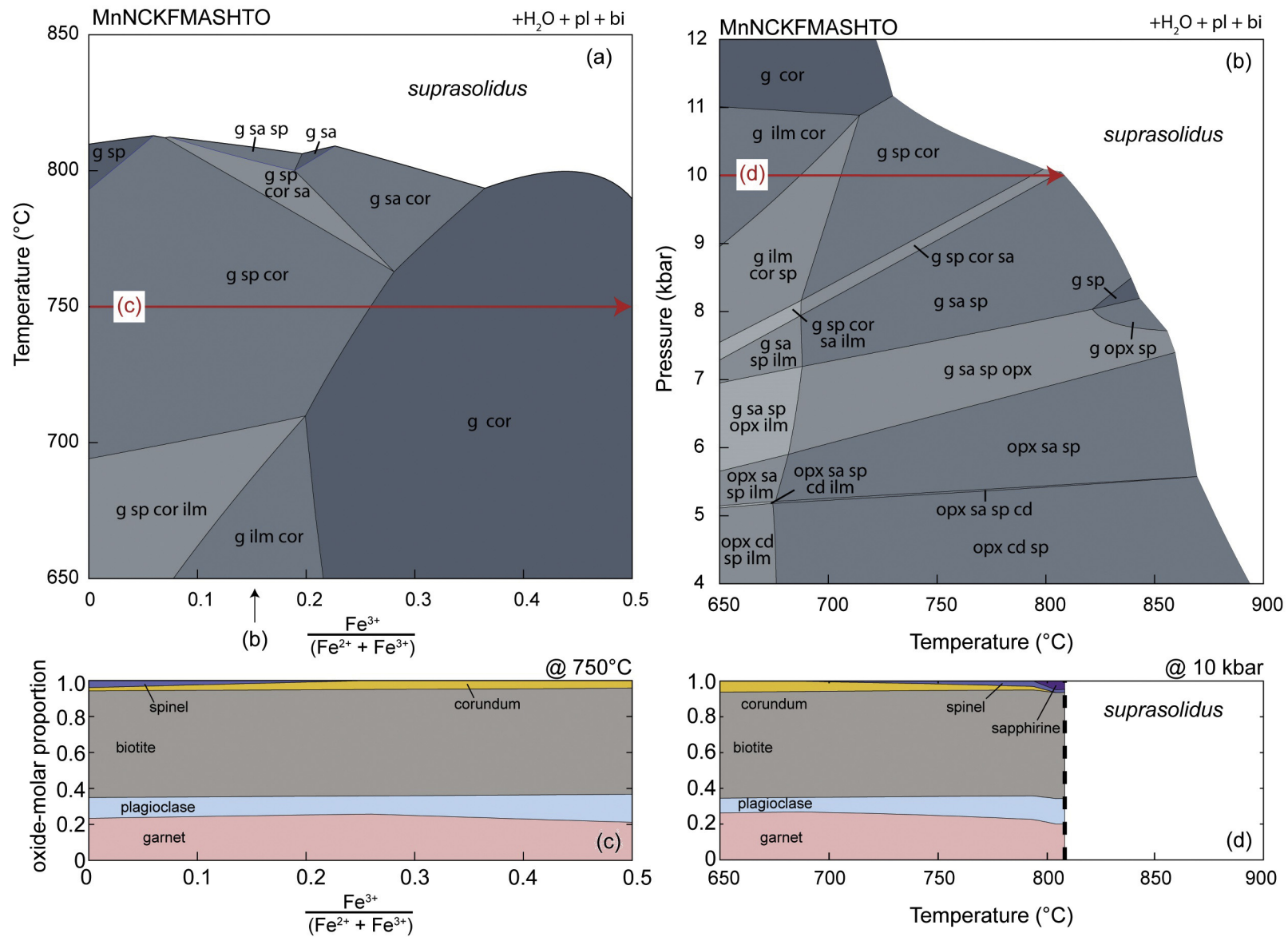
Figure 16. Maniitsoq ruby mica schist (sample 464). (a) Temperature-composition diagram for various ratios of ferric to ferrous iron for the ruby mica schist from Maniitsoq calculated at a fixed pressure of 10 kbar. (b) Pressure-temperature phase diagram for the ruby mica schist from Maniitsoq. (c) Composition-mode diagram illustrating the slight increase in the mode of corundum at the expense of spinel towards more oxidized compositions. (d) Temperature-mode diagram showing the decrease in the predicted mode of corundum towards higher temperatures due to the growth of spinel and sapphirine. Note that this particular sample is relatively silica-rich and has the lowest Al_2O_3 content of any of the studied corundum-bearing rocks. This is clearly reflected by the low corundum mode and the sample likely marks the lower boundary for composition that stabilize corundum. However, the adjacent ruby mica sample (463) has the highest Al_2O_3 and lowest SiO_2 of any of the studied rocks, and would thus likely have a corundum mode larger than even Storø sample 11801 of 20%.
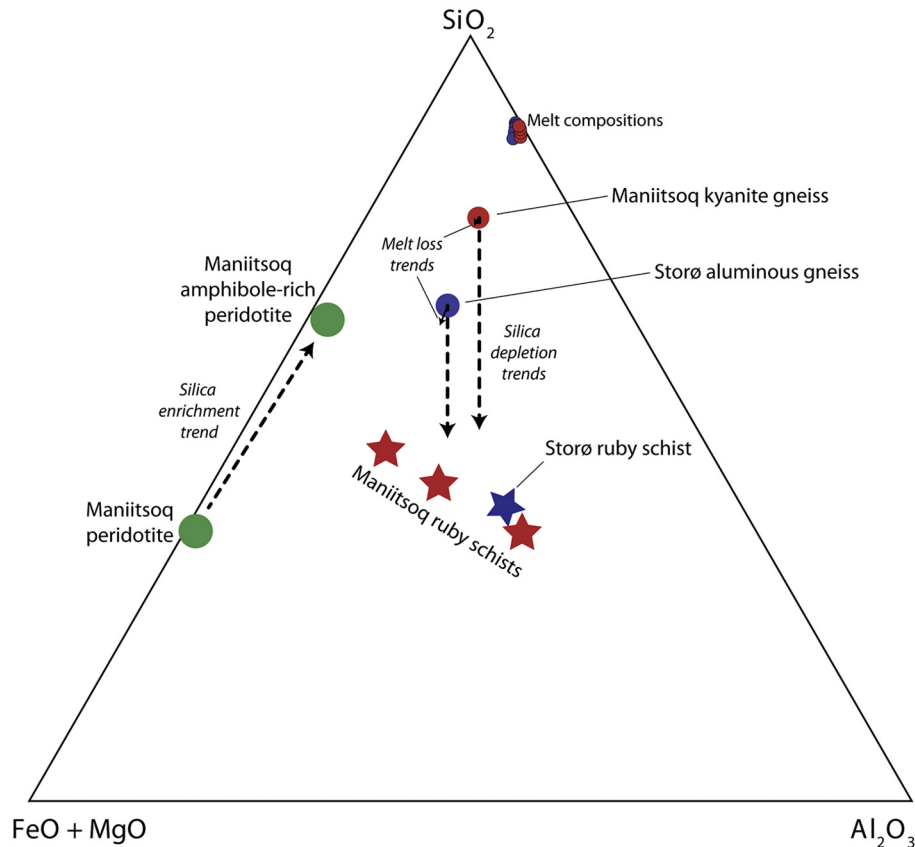
Figure 17. Ternary diagram showing (FeO + MgO) vs. SiO$_2$ vs. Al$_2$O$_3$ (oxides are plotted as molar proportions) for the rocks involved in the corundum formation at Maniitsoq and Storø. The melt loss vectors (barely visible) are the appropriate length for the extraction of up to 10% melt; the composition and proportion of melt for the Maniitsoq kyanite-schist and Storø aluminous gneiss were calculated with Thermocalc at 700, 750, 800, 850 and 900 °C, respectively, although they do not different significantly. Note that the large enrichment in silica going from the most refractory peridotite (sample 455) to the most amphibole-rich peridotite (sample 466) at the Maniitsoq corundum locality. This enrichment in silica can easily account for the corresponding loss that is observed going from the kyanite gneiss to the corundum mica schists. Ultramafic rocks are shown in green symbols, Maniitsoq rocks in red, and Storø rocks in blue.

and Maniitsoq using median and measured compositions of key units to evaluate the general framework of corundum and quartz stability during metamorphism. Therefore, the results here are not necessarily representative of all bulk compositions that can host ruby. For example, modelling of the Storø aluminous gneiss compositions predicts a few volume percent corundum in the rocks. However, there are occurrences in the Storø region where corundum modes can locally reach 10%–20% (Fig. 4). Nonetheless, the general reactions and phase assemblages modelled provide some important general criteria for ruby exploration in metamorphic rocks.

We focus on SiO$_2$ depletion and, to a lesser extent, the ratio of ferric to ferrous iron in the bulk composition to explore the stability of corundum. However, it is unlikely that SiO$_2$ is the only mobile component in metasomatic systems that contain ruby and the geochemistry of the rocks from Storø and Maniitsoq may indicate Al$_2$O$_3$ mobility. Riesco et al. (2004) demonstrated that SiO$_2$ and Na$_2$O depletion affect the stability of corundum in metapelites from the Eastern Alps. Furthermore, we did not investigate the role of fluid composition on the subsolidus stability of corundum-bearing assemblages, but CO$_2$-rich fluids may be important in some ruby occurrences in graphite-rich host rocks, such as those found in southeast Kenya (e.g., Mercier et al., 1999). Schumacher et al. (2011) suggested that high pH at low Eh might have played a role in the formation of the ruby in the Fiskenæsset complex from alkaline fluids (Keulen et al., 2014).

6.3. Implications for mineral exploration

There are five main implications of the phase equilibria modelling for ruby exploration in metamorphic terrains. Firstly, if quartz is present then corundum is not expected to be stable. Quartz-bearing rocks should not be prioritized for ruby exploration. Secondly, less SiO$_2$ depletion of the bulk composition is required at higher temperatures to stabilize corundum (Figs. 11a and 12a). Therefore, in general, higher-grade metamorphic terrains are potentially better targets for ruby exploration than low grade ones. However, when spinel and sapphirine are stabilized at higher temperatures, they grow at the expense of corundum. The association of sapphirine and ruby has been documented in deposits at Qeqertarsuatsiaat (Fiskenæsset) in SW Greenland (e.g., Herd et al., 1969) and in southeast Kenya (Mercier et al., 1999). Thirdly, the main corundum producing reaction includes sillimanite or kyanite as a reactant. Sillimanite (or kyanite) bearing rocks should be targeted because they may have enough Al$_2$O$_3$ to stabilize corundum if some SiO$_2$ was locally mobilized out of them. Fourthly, aluminous protoliths should be targeted because more mafic rocks will not produce corundum, even with extreme SiO$_2$ depletion (Fig. 10). Finally, a geological mechanism to deplete the aluminous protolith in SiO$_2$ is required. At the Storø and Maniitsoq ruby occurrences, this is accomplished by the juxtaposition of low silica ultramafic rocks with aluminous gneisses. The juxtaposition of ultramafic rocks and aluminous rocks has also been proposed as a model for ruby-formation in the Fiskenæsset complex (Schumacher et al., 2011; Keulen et al., 2014).

Ultramafic rocks are relatively common in the region between Nuuk and Maniitsoq (e.g., Szilas et al., 2015), and as documented in the present study (see Section 3), such rocks may indeed become tectonically juxtaposed with aluminous supracrustal rocks and result in the formation of corundum during subsequent high-grade metamorphism. The association between ultramafic rocks and corundum in aluminous supracrustal rocks in metamorphic terrains has also been observed in Proterozoic and Phanerozoic metamorphic terrains (Mercier et al., 1999; Riesco et al., 2005).

We recommend that future work on the Storø and Maniitsoq corundum localities should investigate the zoning patterns of the euhedral rubies and examine the occurrence of sapphire vs. sapphirine in these rocks, which are easily mistaken in the field. Detailed *in situ* trace element and oxygen isotope measurements are also recommended to expand the current data base for corundum from Greenland.

7. Conclusions

Ruby-bearing rocks at Storø and Maniitsoq are found at the contact between ultramafic rocks and aluminous gneisses. Trace element chemical composition of the ruby-bearing rocks indicate that their protoliths were similar to the adjacent aluminous gneisses, which are inferred to have a sedimentary origin. Tectonic juxtaposition of these rock types and metamorphism created a chemical potential gradient in silica that drove desilicification of the aluminous gneisses and silicification of the ultramafic rocks. The ultramafic rocks also appear to be important as a source of trace elements needed for the coloring of corundum (ruby/sapphire), such as chromium and titanium.

Phase equilibria modeling of the aluminous gneisses indicates that silica depletion during metamorphism can destabilize quartz and grow corundum at both localities at the estimated $P-T$ conditions. However, the modeling also predicts that too high temperature (>750 °C) promotes the stability of sapphirine at the expense of corundum, and too low pressure (<6 kbar) stabilizes cordierite. Changes in iron speciation (Fe^{2+}/Fe^{3+}) have only a minor effect on the predicted mode of corundum at the estimated peak metamorphic conditions.

Aluminum appears to have been enriched in the corundum-bearing rocks relative to their metasedimentary precursor rocks. Melt extraction cannot reproduce the measured compositions but Al-hydroxide complexes or Na-Al-Si-O polymers may have transported Al by metasomatic reactions in the deep crust. An overall high prospectivity of corundum in Archean greenstone belts is thus found in amphibolite-facies terrains hosting sillimanite- or kyanite-rich aluminous gneisses, which are spatially related to metaperidotites as demonstrated by ruby-bearing rocks at Storø and Maniitsoq.

Acknowledgements

References

Appel, C.C., Appel, P.W.U., Rollinson, H.R., 2002. Complex chromite textures reveal the history of an early Archaean layered ultramafic body in West Greenland. Mineralogical Magazine 66, 1029–1041.

Bach, W., Klein, F., 2009. The petrology of seafloor rodingites: insights from geochemical reaction path modeling. Lithos 112, 103–117.

Berthelsen, A., 1962. Structural studies in the pre-Cambrian of Western Greenland. Geological Survey of Greenland Bulletin 31, 47.

Boger, S.D., White, R.W., Schulte, B., 2012. The importance of iron speciation (Fe^{2+}/Fe^{3+}) in determining mineral assemblages: an example from the high-grade aluminous metapelites of southeastern Madagascar. Journal of Metamorphic Geology 30, 997–1018.

Bottrill, R., 1998. A corundum-quartz assemblage in altered volcanic rocks, Bond range, Tasmania. Mineralogical Magazine 62, 325–332.

Brown, M., 2008. Characteristic thermal regimes of plate tectonics and their metamorphic imprint throughout Earth history: when did Earth first adopt a plate tectonics mode of behavior. Geological Society of America Special Papers 440, 97–128.

Cartwright, I., Barnicoat, A.C., 1986. The generation of quartz-normative melts and corundum-bearing restites by crustal anatexis: petrogenetic modelling based on an example from the Lewisian of North-West Scotland. Journal of Metamorphic Geology 4, 79–99.

Clemens, J.D., Vielzeuf, D., 1987. Constraints on melting and magma production in the crust. Earth and Planetary Science Letters 86, 287–306.

Collins, W.J., Van Kranendonk, A.M., Teyssier, C., 1998. Partial convective overturn of Archaean crust in the east Pilbara Craton, Western Australia: driving mechanisms and tectonic implications. Journal of Structural Geology 20, 1405–1424.

Danmarks og Grønlands Geologiske Undersøgelse Rapport 2005/42. In: Hollis, J.A. (Ed.), 2005. Greenstone Belts in the Central Godthåbsfjord Region, Southern West Greenland: Geochemistry, Geochronology and Petrography Arising from 2004 Field Work, and Digital Map Data, p. 215.

Dhuime, B., Hawkesworth, C.J., Cawood, P.A., Storey, C.D., 2012. A change in the geodynamics of continental growth 3 billion years ago. Science 335, 1334–1336.

Diener, J.F.A., Powell, R., 2010. Influence of ferric iron on the stability of mineral assemblages. Journal of Metamorphic Geology 28, 599–613.

Dyck, B., Reno, B.L., Kokfelt, T.F., 2015. The Majorqaq Belt: a record of Neoarchaean orogenesis during final assembly of the North Atlantic Craton, southern West Greenland. Lithos 220, 253–271.

Frost, B.R., 1985. On the stability of sulfides, oxides, and native metals in serpentinite. Journal of Petrology 26, 31–61.

Garde, A.A., 1997. Accretion and evolution of an Archaean high-grade grey gneiss-amphibolite complex: the Fiskefjord area, southern West Greenland. Geology of Greenland Survey Bulletin 177, 115.

Garde, A.A., 2007. A mid-Archaean island arc complex in the eastern Akia terrane, Godthåbsfjord, southern West Greenland. Journal of the Geological Society 164, 565–579.

Garde, A., Marker, M., 1988. Corundum crystals with blue-red color zoning near Kangerdluarssuk, Sukkertoppen district, West Greenland. Rapport Grønlands Geologiske Undersøgelse 140, 46–49.

Garde, A.A., Friend, C.R.L., Nutman, A.P., 2000. Rapid maturation and stabilization of the middle Archaean continental crust: the Akia terrane, southern West Greenland. Bulletin of the Geological Society of Denmark 47, 1–27.

Garde, A.A., Dyck, B., Esbensen, K.H., Johansson, L., Möller, C., 2014. The Finnefjeld domain, Maniitsoq structure, West Greenland: differential rheological features and mechanical homogenisation in response to impacting? Precambrian Research 255, 791–808.

Garnier, V., Giuliani, G., Ohnenstetter, D., Fallick, A.E., Dubessy, J., Banks, D., Bakhsh, K.A., 2008. Marble-hosted ruby deposits from Central and Southeast Asia: towards a new genetic model. Ore Geology Reviews 34, 169–191.

Giuliani, G., Fallick, A.E., Garnier, V., France-Lanord, C., Ohnenstetter, D., Schwarz, D., 2005. Oxygen isotope composition as a tracer for the origins of rubies and sapphires. Geology 33, 249–252.

Giuliani, G., Ohnenstetter, D., Fallick, A.E., Groat, L., Fagan, A.J., 2014. Chapter 2: the geology and genesis of gem corundum deposits. In: Groat, L.A. (Ed.), Geology of Gem Deposits, second ed., 44. Mineralogical Association of Canada Short Course Series, pp. 29–112.

Goliani, P.R., 1989. Sillimanite-corundum deposits of Sonapahar, Meghalaya, India: a metamorphosed Precambrian paleosol. Precambrian Research 43, 175–189.

Grant, J.A., 1986. The isocon diagram; a simple solution to Gresens' equation for metasomatic alteration. Economic Geology 81, 1976–1982.

Green, E.C.R., White, R.W., Diener, J.F.A., Powell, R., Holland, T.J.B., Palin, R.M., 2016. Activity-composition relations for the calculation of partial melting equilibria in metabasic rocks. Journal of Metamorphic Geology 34, 845–869.

Groat, L.A., Turner, D.J., Evans, R.J., 2014. 13.23 gem deposits. In: Holland, H.D. (Ed.), Treatise on Geochemistry, second ed., 13, pp. 595–622.

Guiraud, M., Kienast, J.R., Ouzegane, K., 1996. Corundum-quartz-bearing assemblage in the Ihouhaouene area (In Ouzzal, Algeria). Journal of Metamorphic Geology 14, 755–761.

Guiraud, M., Powell, R., Rebay, G., 2001. H2O in metamorphism and unexpected behaviour in the preservation of metamorphic mineral assemblages. Journal of Metamorphic Geology 19, 445–454.

Hamilton, W.B., 2011. Plate tectonics began in Neoproterozoic time, and plumes from deep mantle have never operated. Lithos 123, 1–20.

Harlov, D.E., Milke, R., Gottschalk, M., 2008. Metastability of sillimanite relative to corundum and quartz in the kyanite stability field: Competition between stable and metastable reactions. American Mineralogist 93, 608–617.

Harrison, T.M., Blichert-Toft, J., Müller, W., Albarede, F., Holden, P., Mojzsis, S.J., 2005. Heterogeneous Hadean hafnium: evidence of continental crust at 4.4 to 4.5 Ga. Science 310, 1947–1950.

Herd, R.K., Windley, B.F., Ghisler, M., 1969. The mode of occurrence and petrogenesis of the sapphirine-bearing and associated rocks of West Greenland. Geological Survey of Greenland Report 24, 44.

Hoffmann, J.E., Svahnberg, H., Piazolo, S., Scherstén, A., Münker, C., 2012. The geodynamic evolution of Mesoarchean anorthosite complexes inferred from the Naajat Kuuat Complex, southern West Greenland. Precambrian Research 196, 149–170.

Holland, T.J.B., Powell, R., 2011. An improved and extended internally consistent thermodynamic dataset for phases of petrological interest, involving a new equation of state for solids. Journal of Metamorphic Geology 29, 333–383.

Hopkins, M., Harrison, T.M., Manning, C.E., 2008. Low heat flow inferred from >4 Gyr zircons suggests Hadean plate boundary interactions. Nature 456, 493–496.

Huang, W.-L., Wyllie, P., 1973. Melting relations of muscovite-granite to 35 kbar as a model for fusion of metamorphosed subducted oceanic sediments. Contributions to Mineralogy and Petrology 42, 1–14.

Huang, H., Fryer, B.J., Polat, A., Pan, Y., 2014. Amphibole, plagioclase and clinopyroxene geochemistry of the Archean Fiskenæsset Complex at Majorqap qâva, southwestern Greenland: implications for Archean petrogenetic and geodynamic processes. Precambrian Research 247, 64–91.

Jenner, F.E., Bennett, V.C., Nutman, A.P., Friend, C.R., Norman, M.D., Yaxley, G., 2009. Evidence for subduction at 3.8 Ga: geochemistry of arc-like metabasalts from the southern edge of the Isua Supracrustal Belt. Chemical Geology 261, 83–98.

Jennings, E.S., Holland, T.J., 2015. A simple thermodynamic model for melting of peridotite in the system NCFMASOCr. Journal of Petrology 56, 869–892.

Kelsey, D.E., Hand, M., 2015. On ultrahigh temperature crustal metamorphism: phase equilibria, trace element thermometry, bulk composition, heat sources, timescales and tectonic settings. Geoscience Frontiers 6, 311–356.

Kerrick, D.M., 1988. Al2SiO5-bearing segregations in the Lepontine Alps, Switzerland: aluminum mobility in metapelites. Geology 16, 636–640.

Kessel, R., Schmidt, M.W., Ulmer, P., Pettke, T., 2005. Trace element signature of subduction-zone fluids, melts and supercritical liquids at 120-180 km depth. Nature 437, 724–727.

Keulen, N., Kalvig, P., 2013. Fingerprinting of corundum (ruby) from Fiskenaesset, West Greenland. Geological Survey Denmark Greenland Bulletin 28, 53–56.

Keulen, N., Schumacher, J.C., Næraa, T., Kokfelt, T.F., Scherstén, A., Szilas, K., Van Hinsberg, V.J., Schlatter, D.M., Windley, B.F., 2014. Meso- and Neoarchaean geological history of the Bjørnesund and Ravns Storø Supracrustal Belts, southern West Greenland: Settings for gold enrichment and corundum formation. Precambrian Research 254, 36–58.

Klein, F., Bach, W., McCollom, T.M., 2013. Compositional controls on hydrogen generation during serpentinization of ultramafic rocks. Lithos 178, 55–69.

Knudsen, C., Van Gool, J.A., Østergaard, C., Hollis, J.A., Rink-Jørgensen, M., Persson, M., Szilas, K., 2007. Gold-hosting supracrustal rocks on Storø, southern West Greenland: lithologies and geological environment. Geological Survey of Denmark and Greenland Bulletin 13, 41–44.

Komiya, T., Yamamoto, S., Aoki, S., Sawaki, Y., Ishikawa, A., Tashiro, T., Collerson, K.D., 2015. Geology of the Eoarchean, >3.95 Ga, Nulliak supracrustal rocks in the Saglek Block, northern Labrador, Canada: the oldest geological evidence for plate tectonics. Tectonophysics 662, 40–66.

Lowry, D., Appel, P.W.U., Rollinson, H.R., 2003. Oxygen isotopes of an early Archaean layered ultramafic body, southern West Greenland: implications for magma source and post-intrusion history. Precambrian Research 126, 273–288.

Manning, C.E., 2006. Mobilizing aluminum in crustal and mantle fluids. Journal of Geochemical Exploration 89, 251–253.

McGregor, V.R., Friend, C.R.L., 1992. Late Archean prograde amphibolite-to granulite-facies relations in the Fiskenæsset region, southern West Greenland. The Journal of Geology 100, 207–219.

Mercier, A., Debat, P., Saul, J.M., 1999. Exotic origin of the ruby deposits of the Mangari area in SE Kenya. Ore Geology Reviews 14, 83–104.

Myers, J.S., 1985. Stratigraphy and structure of the Fiskenæsset complex, southern West Greenland. Bulletin Grønlands Geologiske Undersøgelse 150, 72.

Nutman, A.P., McGregor, V.R., Friend, C.R., Bennett, V.C., Kinny, P.D., 1996. The Itsaq gneiss complex of southern West Greenland; the world's most extensive record of early crustal evolution (3900-3600 Ma). Precambrian Research 78, 1–39.

Nutman, A.P., Christiansen, O., Friend, C.R., 2007. 2635 Ma amphibolite facies gold mineralization near a terrane boundary (suture?) on Storø, Nuuk region, southern West Greenland. Precambrian Research 159, 19–32.

Nutman, A.P., Bennett, V.C., Friend, C.R., 2015. The emergence of the Eoarchaean proto-arc: evolution of a c. 3700 Ma convergent plate boundary at Isua, southern West Greenland. Geological Society, London, Special Publications 389, 113–133.

Oelkers, E.H., Scott, J., Devidal, J.-L., 1994. The effect of aluminium, pH, and chemical affinity on rates of aluminosilicate dissolution reactions. Geochimica et Cosmochimica Acta 58, 2011–2014.

Palke, A.C., Renfro, N.D., Berg, R.B., 2017. Melt inclusions in alluvial sapphires from Montana, USA: formation of sapphires as a restitic component of lower crustal melting? Lithos 278–281, 43–53.

Palme, H., O'Neill, H.S.C., 2003. Cosmochemical estimates of mantle composition. Treatise on Geochemistry 2, 568.

Persson, M., 2007. Metamorphic and Geochronological Evolution of the Au-bearing Rocks on Central Storø, Nuuk Region, West Greenland. Copenhagen University (unpublished M.Sc. thesis).

Polat, A., Hofmann, A.W., Rosing, M.T., 2002. Boninite-like volcanirocks in the 3.7-3.8 Ga Isua greenstone belt, West Greenland: geochemical evidence for intra-oceanic subduction zone processes in the early Earth. Chemical Geology 184, 231–254.

Polat, A., Frei, R., Appel, P.W.U., Dilek, Y., Fryer, B., Ordóñez-Calderón, J.C., Yang, Z., 2008. The origin and compositions of Mesoarchean oceanic crust: evidence from the 3075 Ma Ivisaartoq greenstone belt, SW Greenland. Lithos 100, 293–321.

Polat, A., Appel, P.W., Fryer, B., Windley, B., Frei, R., Samson, I.M., Huang, H., 2009. Trace element systematics of the Neoarchean Fiskenæsset anorthosite complex and associated meta-volcanic rocks, SW Greenland: evidence for a magmatic arc origin. Precambrian Research 175, 87–115.

Polat, A., Fryer, B.J., Samson, I.M., Weisener, C., Appel, P.W., Frei, R., Windley, B.F., 2012. Geochemistry of ultramafic rocks and hornblendite veins in the Fiskenæsset layered anorthosite complex, SW Greenland: evidence for hydrous upper mantle in the Archean. Precambrian Research 214, 124–153.

Pornwilard, M.M., Hansawek, R., Shiowatana, J., Siripinyanond, A., 2011. Geographical origin classification of gem corundum using elemental fingerprint analysis by laser ablation inductively coupled plasma mass spectrometry. International Journal of Mass Spectrometry 306, 57–62.

Porto, S.P.S., Krishnan, R.S., 1967. Raman effect of corundum. The Journal of Chemical Physics 47, 1009–1012.

Powell, R., Holland, T.J.B., 1988. An internally consistent dataset with uncertainties and correlations: 3. Applications to geobarometry, worked examples and a computer program. Journal of Metamorphic Geology 6, 173–204.

Ramberg, H., 1948. On sapphrinie-bearing rocks in the vicinity of Sukkertoppen (West Greenland). Geological Survey of Greenland Bulletin 1, 32.

Reimold, W.U., Gibson, R.L., Koeberl, C., 2013. Comment on "Searching for giant, ancient impact structures on Earth: the Mesoarchaean Maniitsoq structure, West Greenland" by Garde et al. Earth and Planetary Science Letters 369, 333–335.

Reimold, W.U., Ferrière, L., Deutsch, A., Koeberl, C., 2014. Impact controversies: impact recognition criteria and related issues. Meteoritics and Planetary Science 49, 723–731.

Riesco, M., Stüwe, K., Reche, J., 2005. Formation of corundum in metapelites around ultramafic bodies. An example from the Saualpe region, Eastern Alps. Mineralogy and Petrology 83, 1–25.

Riesco, M., Stüwe, K., Reche, J., Martinez, F.J., 2004. Silica depleted melting of pelites. Petrogenetic grid and application to the Susqueda Aureole, Spain. Journal of Metamorphic Geology 22, 475–494.

Scherstén, A., Szilas, K., Creaser, R.A., Næraa, T., Van Gool, J.A., Østergaard, C., 2012. Re-Os and U-Pb constraints on gold mineralisation events in the Meso- to Neoarchaean Storø greenstone belt, Storø, southern West Greenland. Precambrian Research 200, 149–162.

Schumacher, J.C., Van Hinsberg, V.J., Keulen, N., 2011. Metamorphism in Supracrustal and Ultramafic Rocks in Southern West and South-West Greenland 64-61.5 N. Geological Survey of Denmark and Greenland Report 2011/6, p. 30.

Shaw, R.K., Arima, M., 1998. A corundum-quartz assemblage from the Eastern Ghats Granulite Belt, India: evidence for high P-T metamorphism? Journal of Metamorphic Geology 16, 189–196.

Shor, R., Weldon, R., 2009. Ruby and Sapphire production and distribution: a quarter Century of change. Gems and Gemology 45, 236–259.

Simonet, C., Fritsch, E., Lasnier, B., 2008. A classification of gem corundum deposits aimed towards gem exploration. Ore Geology Reviews 34 (1), 127–133.

Smithies, R.H., Van Kranendonk, M.J., Champion, D.C., 2007. The Mesoarchean emergence of modern-style subduction. Gondwana Research 11, 50–68.

Sørensen, H., 1954. The border relations of the dunite at Siorarssuit, Sukkertoppen district, West Greenland. Geological Survey of Greenland Bulletin 6, 47.

Stern, R.J., 2008. Modern-style plate tectonics began in Neoproterozoic time: an alternative interpretation of Earth's tectonic history. Geological Society of America Special Papers 440, 265–280.

Sutherland, F.L., Hoskin, P.W., Fanning, C.M., Coenraads, R.R., 1998. Models of corundum origin from alkali basaltic terrains: a reappraisal. Contributions to Mineralogy and Petrology 133, 356–372.

Szilas, K., Garde, A.A., 2013. Mesoarchaean aluminous rocks at Storø, southern West Greenland: new age data and evidence of premetamorphic seafloor weathering of basalts. Chemical Geology 354, 124–138.

Szilas, K., Hoffmann, J.E., Scherstén, A., Rosing, M.T., Kokfelt, T.F., Windley, B.F., Van Hinsberg, V.J., Næraa, T., Keulen, N., Frei, R., Münker, C., 2012. Complex calc-alkaline volcanism recorded in Mesoarchaean supracrustal belts north of Frederikshåb Isblink, southern West Greenland: Implications for subduction zone processes in the early Earth. Precambrian Research 208–211, 90–123.

Szilas, K., Hoffmann, J.E., Scherstén, A., Kokfelt, T.F., Münker, C., 2013. Archaean andesite petrogenesis: insights from the Grædefjord Supracrustal Belt, southern West Greenland. Precambrian Research 236, 1–15.

Szilas, K., Hoffmann, J.E., Münker, C., Dziggel, A., Rosing, M.T., 2014a. Eoarchean within-plate basalts from southwest Greenland: Comment. Geology 42, e330.

Szilas, K., Van Gool, J.A., Scherstén, A., Frei, R., 2014b. The Neoarchaean Storø Supracrustal Belt, Nuuk region, southern West Greenland: an arc-related basin with continent-derived sedimentation. Precambrian Research 247, 208–222.

Szilas, K., Kelemen, P.B., Bernstein, S., 2015. Peridotite enclaves hosted by Mesoarchaean TTG-suite orthogneisses in the Fiskefjord region of southern West Greenland. GeoResJ 7, 22–34.

Szilas, K., Maher, K., Bird, D.K., 2016. Aluminous gneiss derived by weathering of basaltic source rocks in the Neoarchean Storø Supracrustal Belt, southern West Greenland. Chemical Geology 441, 63–80.

Szilas, K., Tusch, J., Hoffmann, J.E., Garde, A.A., Münker, C., 2017. Hafnium isotope constraints on the origin of Mesoarchaean andesites in southern West Greenland, North Atlantic craton. In: Halla, J., Whitehouse, M.J., Ahmad, T., Bagai, Z. (Eds.), Crust-Mantle Interactions and Granitoid Diversification: Insights from Archaean Cratons, 449. Geological Society, London, Special Publications, pp. 19–38.

Szilas, K., Van Hinsberg, V.J., McDonald, I., Næraa, T., Rollinson, H., Adetunji, J., Bird, D., 2018. Highly refractory Archaean peridotite cumulates: petrology and geochemistry of the Seqi Ultramafic complex, SW Greenland. Geoscience Frontiers 9, 681–707.

Thompson, A.B., 1982. Dehydration melting of pelitic rocks and the generation of H_2O-undersaturated granitic liquids. American Journal of Science 282, 1567–1595.

Thirangoon, K., 2008. Ruby and Pink Sapphire from Aappaluttoq, Greenland. Status of On-going Research. Unpublished report for True North Gems Co. In archives of Geological Survey of Denmark and Greenland, GEUS Report File 23642, p. 18.

Van Kranendonk, M.J., Collins, W.J., Hickman, A., Pawley, M.J., 2004. Critical tests of vertical vs. horizontal tectonic models for the Archaean East Pilbara granite-greenstone terrane, Pilbara craton, western Australia. Precambrian Research 131, 173–211.

Van Gool, J.A.M., 2006. Ruby Showings on Storø, 7. Geological Survey of Greenland and Denmark (GEUS). Preliminary report with field notes and geologic map.

Van Gool, J.A.M., Scherstén, A., Østergaard, C., Næraa, T., 2007. Geological Setting of the Storø Gold Prospect Godthåbsfjord Region, Southern West Greenland: Results of Detailed Mapping, Structural Analysis, Geochronology and Geochemistry. Danmarks Grønlands Geologiske Undersøgelse Rapport 2007/83, p. 158.

Watson, E.B., Harrison, T.M., 2005. Zircon thermometer reveals minimum melting conditions on earliest Earth. Science 308, 841–844.

Webb, G., Powell, R., McLaren, S., 2015. Phase equilibria constraints on the melt fertility of crustal rocks: the effect of subsolidus water loss. Journal of Metamorphic Geology 33, 147–165.

White, R.W., Pomroy, N.E., Powell, R., 2005. An in situ metatexite-diatexite transition in upper amphibolite facies rocks from Broken Hill, Australia. Journal of Metamorphic Geology 23, 579–602.

White, R.W., Powell, R., 2002. Melt loss and the preservation of granulite facies mineral assemblages. Journal of Metamorphic Geology 20, 621–632.

White, R.W., Powell, R., Baldwin, J.A., 2008. Calculated phase equilibria involving chemical potentials to investigate the textural evolution of metamorphic rocks. Journal of Metamorphic Geology 26, 181–198.

White, R.W., Powell, R., Holland, T.J.B., Johnson, T.E., Green, E.C.R., 2014a. New mineral activity-composition relations for thermodynamic calculations in metapelitic systems. Journal of Metamorphic Geology 32, 261–286.

White, R.W., Powell, R., Johnson, T.E., 2014b. The effect of Mn on mineral stability in metapelites revisited: new a-x relations for manganese-bearing minerals. Journal of Metamorphic Geology 32, 809–828.

Windley, B.F., Garde, A.A., 2009. Arc-generated blocks with crustal sections in the North Atlantic craton of West Greenland: crustal growth in the Archean with modern analogues. Earth Science Reviews 93, 1–30.